

Temporal trapping of ultrashort pulses enables deterministic optical quantum computation

Ryotatsu Yanagimoto,^{1,*} Edwin Ng,^{1,2} Marc Jankowski,^{1,2} Hideo Mabuchi,¹ and Ryan Hamerly^{2,3,†}

¹*E. L. Ginzton Laboratory, Stanford University, Stanford, California 94305, USA*

²*Physics & Informatics Laboratories, NTT Research, Inc., Sunnyvale, California 94085, USA*

³*Research Laboratory of Electronics, MIT, 50 Vassar Street, Cambridge, MA 02139, USA*

(Dated: March 23, 2022)

The realization of deterministic photon-photon gates is a central goal in optical quantum computation and engineering. While solid-state nonlinear optics offers a scalable, room temperature solution, weak material nonlinearities lead to extremely demanding requirements on optical loss and confinement, which to date have not been realized. In this work, we introduce a novel confinement method, dispersion-engineered temporal trapping, which enhances the nonlinear interaction strength by orders of magnitude by simultaneously confining photons in both time and space. Temporal confinement is imposed by a non-resonant “trap” pulse via cross-phase modulation, realizing a wavelength-scale “flying cavity”. Numerical simulations confirm that temporal trapping confines the multimode nonlinear dynamics to a single-mode subspace, enabling high-fidelity deterministic quantum gate operations. With realistic dispersion engineering and loss figures, we show that temporally trapped ultrashort pulses could achieve strong coupling on near-term nonlinear nanophotonic platforms. Our scheme is compatible with traveling-wave implementations and intracavity time multiplexing, which can further enhance the operation bandwidth and scalability. We expect temporal trapping to open a new path to optical strong coupling, with applications in quantum computing, simulation, and light sources.

INTRODUCTION

Photons are ideal carriers of quantum information, enjoying minimal decoherence even at room temperature, and propagating long distances with low loss at high data rates. These advantages render optics essential to quantum key distribution [1], networking [2], and metrology [3], and have led to significant progress towards optical quantum computation [4–6]. The main challenge to the latter lies in realizing on-demand entangling gates between optical qubits, in light of the weak photon-photon coupling in most materials. The dominant paradigm—linear optical quantum computing (LOQC)—circumvents this problem by utilizing the inherent nonlinearity of measurements [7]. Since the resulting gates are probabilistic [8], LOQC relies on the creation of entangled ancillae [7] or cluster states [9, 10], which suffer from large resource overheads in terms of the number of photons and detectors per gate [11–14].

The inherent difficulty of probabilistic gates has led to sustained interest in so-called nonlinear-optical quantum computing (NLOQC), where deterministic gate operations are implemented coherently through a nonlinear-optical interaction [15–17]. Here, high-fidelity gates are possible in the strong-coupling regime when the nonlinear interaction rate g exceeds the decoherence rate κ , i.e., $g/\kappa \gg 1$. Strong coupling is readily achieved in cavity QED, where resonant two-level systems such as atomic defects mediate strong optical nonlinearities [18–21], but such systems require vacuum and/or cryogenic

temperatures, and challenges with fabrication, yield, and noise have proved daunting despite decades of research. By contrast, bulk material nonlinearities such as $\chi^{(3)}$ and $\chi^{(2)}$ are robust, scalable, and room-temperature, but the optical interaction is much weaker, imposing very demanding requirements on the optical loss (quality factor Q) and confinement (mode volume V). Moreover, to harness the much stronger $\chi^{(2)}$ effect, one has to overcome the challenge of realizing high- Q resonances separated by an octave, for which guided-wave (e.g. ring, disk, Fabry-Perot) resonators are favorable options. Great progress has been achieved to this end in ultra-low-loss thin-film LiNbO₃ (TFLN) [22], which has rendered plausible a near-strong coupling regime $g/\kappa \sim 1$ with ring resonators in the near future [23]. Even with these developments, however, $g/\kappa \gg 1$ remains a challenge owing to the ring’s large mode volume, as the axial dimension remains unconfined. To reach strong coupling, field confinement in two transverse spatial dimensions is not enough. We also need a means to confine light in the third direction—time.

This paper introduces the *temporal trap*, a nonlinear-optical mechanism to confine light in time as well as space. To facilitate trapping, we introduce a strong non-resonant “trap pulse”, which co-propagates with the target fields and introduces a nonlinear phase shift through cross-phase modulation (XPM). Analogous to an optical soliton [24], the trap pulse creates a flying photonic cavity that supports a bound mode formed by the competition between dispersion and nonlinearity, with a mode volume reduced by the trap duty cycle. With appropriate dispersion engineering [25], the bound mode is strongly detuned from the remaining cavity degrees of freedom, ensuring single-mode dynamics that

* ryotatsu@stanford.edu

† rhamerly@mit.edu

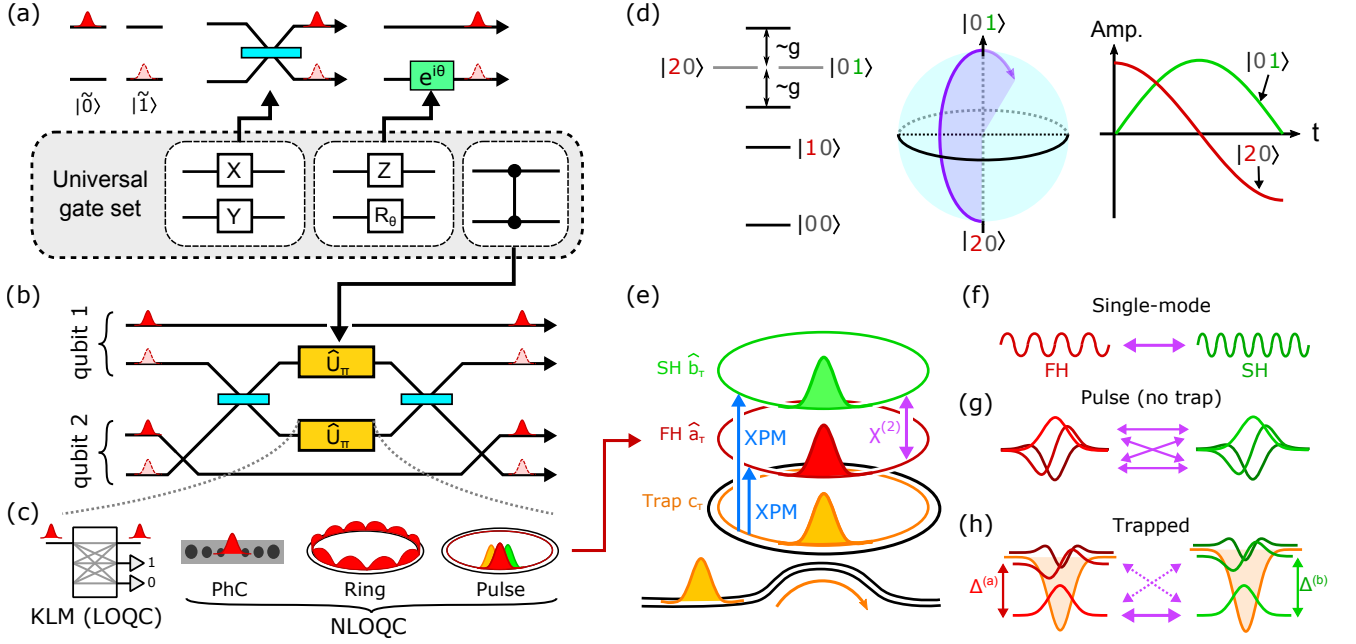


FIG. 1. Universal QC is realized on a dual-rail qubit basis with (a) single-qubit gates based on passive linear optics, and (b) a CZ gate constructed from a Kerr-phase interaction \hat{U}_π inside a Mach-Zehnder interferometer. (c) Potential realizations of \hat{U}_π in LOQC and NLOQC. (d) $\chi^{(2)}$ -mediated \hat{U}_π gate: coupling between the FH state $|20\rangle$ and the SH state $|01\rangle$ leads to Rabi oscillations, imparting a nonlinear phase shift on the signal field. (e) Temporal trap: the $\chi^{(2)}$ interaction between FH and SH fields is enhanced when confined to ultrashort pulses through trap-pulse XPM. Untrapped dynamics are either (f) CW and single-mode or (g) pulsed and multimode, depending on the dispersion. (h) Temporal trapping imposes single-mode dynamics by breaking the degeneracy between trapped and untrapped modes, the former protected by an energy gap Δ .

circumvent the inherent challenges of pulsed nonlinear quantum gates highlighted in Ref. [26, 27]. As a result, we show that high-fidelity two-qubit entangling gate (i.e., controlled-Z gate) operation is possible, providing a roadmap to fully deterministic NLOQC. The tight temporal confinement also significantly increases nonlinear coupling strength, with which we find $g/\kappa \gtrsim 10$ is plausible for realistic nonlinearities and propagation losses on TFLN photonics. Our prescription using temporal traps supports time multiplexing [28], enabling significant parallelism in a single cavity, and is compatible with existing proposals in NLOQC [15–17], where it both provides a means to resolve the otherwise unavoidable multimode interactions and also enhances nonlinear coupling strength.

OPTICAL QUANTUM COMPUTING IN A TEMPORAL TRAP

Single-photon qubits are a leading approach for optical quantum computation [4]. The dual-rail basis, which encodes a state in polarization [29], time-bin [30], or path [31, 32], is a particularly attractive choice, since all single-qubit gates reduce to linear optics (Fig. 1(a)). To complete the gate set, we also need a two-qubit entangling gate, e.g., a controlled-Z (CZ) gate. The most common prescription, shown in Fig. 1(b), implements CZ

with a Mach-Zehnder interferometer (MZI) that encloses a Kerr-phase interaction:

$$\hat{U}_\pi [c_0 |0\rangle + c_1 |1\rangle + c_2 |2\rangle] = c_0 |0\rangle + c_1 |1\rangle - c_2 |2\rangle, \quad (1)$$

where $|n\rangle$ represents the n -photon Fock state. This circuit exploits the Hong-Ou-Mandel effect [33] to ensure that two photons are incident on the \hat{U}_π gate only when the qubits are in the logical state $|\bar{1}\bar{1}\rangle$, implementing the π -phase shift exclusively for this state.

To implement \hat{U}_π (Fig. 1(c)), one can employ the Knill-Laflamme-Milburn (KLM) scheme, which forms the basis for LOQC [7, 8]. KLM suffers from a low success probability of $2/27$ for the CZ gate, and deterministic operations require the preparation of an initial highly entangled state, e.g., a cluster state [9, 10], at significant overhead [12]. In light of these difficulties, here we focus on NLOQC, which aims at deterministic gate operations using coherent nonlinear dynamics [15–17]. For instance, unitary evolution under a single-mode Kerr nonlinearity $\hat{H}_{\text{gate}} = \frac{1}{2}\chi\hat{a}^{\dagger 2}\hat{a}^2$ for time $t_\pi = \pi\chi^{-1}$ implements \hat{U}_π . To leverage the much stronger quadratic nonlinearity, we instead consider a single-mode degenerate $\chi^{(2)}$ Hamiltonian

$$\hat{H}_{\text{gate}} = \frac{g}{2}(\hat{a}^2\hat{b}^\dagger + \hat{a}^{\dagger 2}\hat{b}), \quad (2)$$

where \hat{a} and \hat{b} are annihilation operators for the signal (fundamental harmonic, FH) and pump (second

	Q_a	Q_b	\tilde{V}	d_{eff}	g/κ	Modes
PhC*	10^6	10^3	1	33 pm/V	0.03	1
Ring [†]	10^7	10^7	2000	21 pm/V	0.1	1
Pulse [‡]	10^7	10^7	20	21 pm/V	1	$\gg 1$

TABLE I. Typical estimates of Q , V , and cooperativity for competing confinement mechanisms. LiNbO₃, $\lambda = 1.55 \mu\text{m}$. *Doubly-resonant PhC based on intersecting nanobeams, BIC, or nanopillars [34–37]. [†]Ring circumference 2 mm, quasi phase-matched $d_{\text{eff}} = (2/\pi)d_{33}$, loss $\alpha = 3 \text{ dB/m}$ [22]. [‡]Pulse of width 50 fs, dispersion engineered waveguide.

harmonic, SH) modes, respectively. As shown in Fig. 1(d), the Hamiltonian (2) mediates interactions between the two-photon signal state $|20\rangle$ and the single-photon pump state $|01\rangle$ with coupling strength $g > 0$, resulting in a Rabi oscillation between these two states. Importantly, for an initial state of $|20\rangle$, the system oscillates back to the same state after a period of $t_\pi = \sqrt{2}g^{-1}$ but with an opposite sign, i.e., $-|20\rangle$. As a result, for an initial signal state of $c_0|0\rangle + c_1|1\rangle + c_2|2\rangle$ and a vacuum pump state, unitary evolution under (2) for time t_π implements \hat{U}_π deterministically.

Now, the problem of implementing a CZ gate reduces to the realization of the single-mode $\chi^{(2)}$ Hamiltonian (2) with strong coupling, for which we sketch three possible realizations in Fig. 1(c): a photonic-crystal cavity (PhC), a micro-ring resonator, and our proposed scheme using an ultrashort pulse. For resonators, the cooperativity figure of merit $g/\kappa = g/\sqrt{\kappa_a\kappa_b}$ depends on the Q factor and mode volume as follows:

$$\frac{g}{\kappa} = \sqrt{\frac{4\pi\hbar c d_{\text{eff}}^2}{n^3 \epsilon_0 \lambda^4} \frac{Q_a Q_b}{\tilde{V}}}, \quad (3)$$

where n and d_{eff} are the refractive index and quadratic susceptibility of the medium, and $\tilde{V} = V/(\lambda/n)^3$ is the normalized volume, with $V = |n^3 \int E_b^*(E_a)^2 d^3\vec{x}|^{-2}$, and λ is the wavelength of the FH; see Appendix A for details.

Table I reveals the tradeoff between Q and V in resonator design. In terms of their generic properties, a PhC cavity leverages a wavelength-scale mode volume $V \lesssim (\lambda/n)^3$ with modest $Q \sim 10^6$ ($Q \sim 10^7$ is in principle possible, but at low yield [38–44]). However, as PhCs rely on Bragg scattering for confinement, simultaneous resonance of octave-spanning modes is very difficult, leading to lower quality factors $Q \lesssim 10^4$ at the SH [34–37]. On the other hand, the light in ring resonators is guided by total internal reflection, a geometric effect that is only weakly wavelength-dependent. Therefore, rings can readily resonate modes spanning an octave, with Q factors limited only by waveguide loss. With ion-sliced TFLN, losses of 3 dB/m ($Q = 10^7$) have been achieved [22], and there is a pathway to reach $Q = 10^8$ with process improvements [45–47], which is close to the bulk material limit [48–51]. For the Kerr effect, PhC cavities offer better performance; however, the nonlinearity is too

weak in standard materials to observe strong coupling with reasonable cavity designs (see Appendix A 3). For $\chi^{(2)}$, ring resonators are the superior option. The advent of ultra-low-loss TFLN has led to considerable progress in ring resonators, with recent experiments reaching $g/\kappa \sim 0.01$ [23]; however, the strong-coupling regime $g/\kappa \gg 1$ remains challenging due to the ring’s large mode volume.

This paper studies the third approach: nonlinear enhancement with trapped pulses. The approach is shown in Fig. 1(e), where in addition to the resonant FH and SH fields, we consider a non-resonant “trap” field, generated by an external pulse train, which forms a temporal potential for the resonant, quantum modes. The Hamiltonian for this system takes the form [52]

$$\hat{H} = \underbrace{\frac{r}{2} \int d\tau (\hat{a}_\tau^\dagger \hat{b}_\tau + \hat{a}_\tau^2 \hat{b}_\tau^\dagger)}_{\hat{H}_{\text{NL}}} + \sum_{u \in \{a,b\}} \underbrace{\int d\tau \hat{u}_\tau^\dagger G_u(\tau) \hat{u}_\tau}_{\hat{H}_{a,L}, \hat{H}_{b,L}}, \quad (4)$$

with periodic boundary conditions on $-T/2 \leq \tau \leq T/2$, where T is the cavity round-trip time.

Here, \hat{a}_τ and \hat{b}_τ are, respectively, FH and SH field operators with commutation relations $[\hat{a}_\tau, \hat{a}_{\tau'}^\dagger] = [\hat{b}_\tau, \hat{b}_{\tau'}^\dagger] = \delta(\tau - \tau')$, defined in terms of the fast-time coordinate τ [53] in a co-propagating frame synchronous with the trap field. The term \hat{H}_{NL} represents the $\chi^{(2)}$ interaction, while $\hat{H}_{a,L}$ and $\hat{H}_{b,L}$ are the respective linear terms for the FH and SH. For the latter, $G_u(\tau) = D_u(-i\partial_\tau) + V_u(\tau)$ is a function of the dispersion operator D_u and the trap potential V_u with $u \in \{a,b\}$. As the trapping potential is mediated by XPM, the shape of the temporal trap $V_u(\tau) = -(n_2/n)\omega_u|c_\tau|^2/A$ is determined by the signal frequency ω_u , the trap-pulse power $|c_\tau|^2$, the nonlinear index n_2 , and the mode area A . Taking into account dispersion up to second order and assuming group-velocity matching between FH and SH, $D_u(s) = \omega_{u,0} - \frac{1}{2}(\beta_{u,2}/\beta_1)s^2$, where the first and second terms represent the carrier frequency and the group-velocity dispersion (GVD), respectively. The eigenstates of $\hat{H}_{u,L}$ consist of excitations of normal modes $\Psi_{u,m}(\tau)$ governed by competition between the trap-pulse XPM and GVD, and they are found by solving an eigenmode problem:

$$\underbrace{\left(\omega_{u,0} + \frac{\beta_{u,2}}{2\beta_1} \partial_\tau^2 + V_u(\tau)\right)}_{G_u(\tau)} \Psi_{u,m}(\tau) = \lambda_{u,m} \Psi_{u,m}(\tau). \quad (5)$$

In the absence of a trap ($V_u(\tau) = 0$), (5) admits continuous wave (CW) eigenmodes $\Psi_{u,m}(\tau) \propto e^{2\pi i m \tau/T}$, i.e., the usual normal modes of a cavity. In a typical nanophotonic cavity where $\beta_{u,2}$ is not specifically engineered to be small (see Fig. 1(f)), large energy gaps ($\propto \beta_{u,2}T^{-2}$) between eigenmodes ensure that the nonlinear dynamics involve only a single FH/SH mode pair [23, 54]. This scenario properly realizes Hamiltonian (2), but with weak coupling strength due to the large mode volume. On the other hand, appropriate dispersion

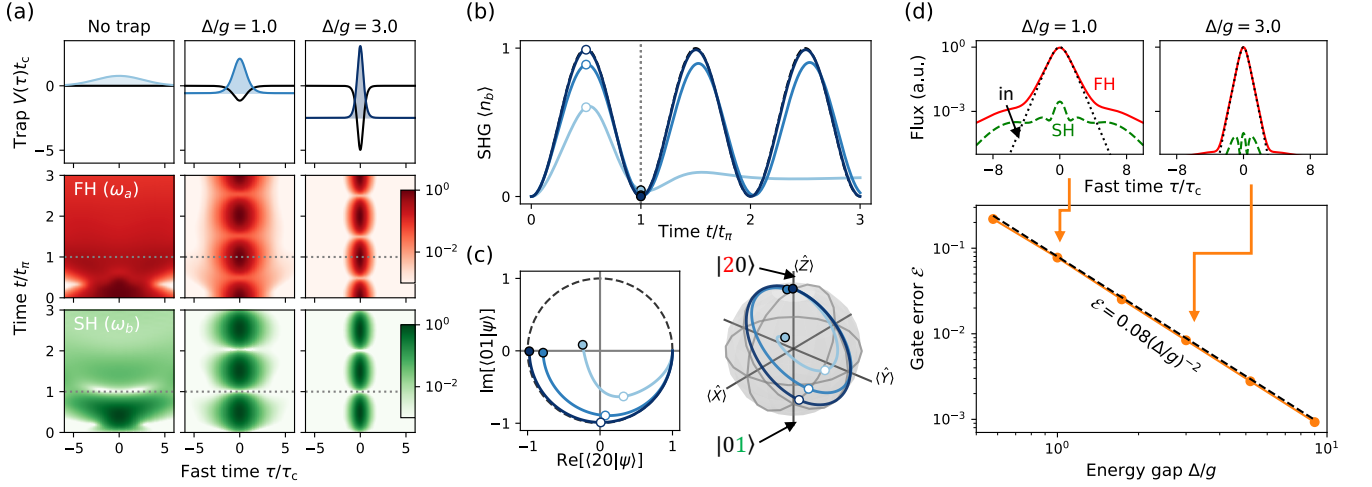


FIG. 2. Two-photon Kerr-phase gate \hat{U}_π with and without temporal trap acting on an initial two-photon FH state $|20\rangle$: (a) initial state and normalized FH / SH flux $\langle \hat{a}_\tau^\dagger \hat{a}_\tau \rangle$, $\langle \hat{b}_\tau^\dagger \hat{b}_\tau \rangle$ as a function of time. The fast-time coordinate is normalized by the characteristic scale $\tau_c = (|\beta_{a,2}|/r\beta_1)^{2/3}$. (b) Rabi oscillations visualized in terms of the total SH photon number as well as (c) a Hilbert-space projection onto $\text{span}(|20\rangle, |01\rangle)$ and rotations on the pseudo-Bloch sphere characterized by the pseudo-Pauli operators $\hat{X} = (\hat{a}^\dagger \hat{b} + \hat{a} \hat{b}^\dagger)/\sqrt{2}$, $\hat{Y} = (\hat{a}^\dagger \hat{b} - \hat{a} \hat{b}^\dagger)/\sqrt{2}i$, $\hat{Z} = \frac{1}{2}\hat{a}^\dagger \hat{a}^2 - \hat{b}^\dagger \hat{b}$ (these project onto Pauli matrices in the two-state subspace). Here we subtract trivial phase rotations induced by the linear dynamics; see Appendix D. (d) Gate error of a CZ gate acting on a reference state $\frac{1}{2}(|\bar{0}\rangle + |\bar{1}\rangle)_1 \otimes (|\bar{0}\rangle + |\bar{1}\rangle)_2$ as a function of the energy gap Δ/g , where subscripts represent the index of qubits. Insets show deviation of output field from the target (input) FH waveform. For all the simulations, we use $\beta_{2,a} = \beta_{2,b}/2$ and $\omega_{b,0} - 2\omega_{a,0} = 0$ with a large enough system size T to avoid boundary effects.

engineering to achieve $\beta_{u,2} \approx 0$ (see Fig. 1(g)) can make all modes nearly degenerate, allowing the cavity to support an ultrashort pulse. However, this modal degeneracy leads to a major problem: although the nonlinear coupling is increased by the pulse confinement, \hat{H}_{NL} is generally all-to-all, as no mechanism exists to force a target pulse shape, leading to intrinsically multimode dynamics unsuitable for high-fidelity qubit operations [26, 27]. These limits highlight the trade-offs between gate fidelity and coupling rate in $\chi^{(2)}$ resonators driven by pulses. Resonators with large $\beta_{u,2}$ driven by long pulses may realize high-fidelity gates with low coupling rates, and conversely, resonators with small $\beta_{u,2}$ driven by short pulses may realize large coupling rates at the cost of reduced gate fidelities. The trap potential eliminates these trade-offs (see Fig. 1(h)): with anomalous dispersion $\beta_{u,2} < 0$, (5) admits at least one *bound eigenmode* $\Psi_{u,0}$, localized in time and protected by an energy gap $\Delta_u = |\lambda_{u,1} - \lambda_{u,0}|$. As a result, all spurious couplings to higher-order eigenmodes are suppressed as off-resonance (i.e., phase-mismatched), and the single-mode dynamics of (2) are recovered, but with a nonlinear coupling boosted by the temporal confinement of $\Psi_{u,0}$.

The importance of single-mode dynamics to high-fidelity quantum gate operation is highlighted in Fig. 2, where we show the propagation of a signal instantiated in a two-photon FH pulse $|20\rangle = 2^{-1/2}(\hat{a}^\dagger)^2|0\rangle$, where $\hat{a} = \int d\tau \Psi^*(\tau) \hat{a}_\tau$ is the annihilation operator for mode $\Psi(\tau)$. To illustrate the limitations of the untrapped

case, we first consider the gate performance of a \hat{U}_π gate using an input Gaussian waveform $\Psi(\tau)$ to a $\chi^{(2)}$ nonlinear resonator. Here, the pulse width and chirp are chosen to minimize the distance from the output state to the target state, where a finite limit is set to the gate time. Even for such optimized pulse parameters (see Appendix D for details), we observe a rapid decay of the Rabi oscillations associated with the SH population as shown in Fig. 2(b). This observed leakage out of the computational subspace is due to the intrinsically multimode structure of the nonlinear polarization used to drive each harmonic, which couples photons into parasitic temporal modes. These results provide evidence that generic quantum nonlinear propagation of a pulse cannot be described by a single-mode model like (2), posing a nontrivial challenge for NLOQC. This problem is often overlooked in the community; most proposals for NLOQC using traveling optical fields assume single-mode interactions of photons [16, 17, 55, 56].

Notably, turning on the temporal trap resolves this problem, restoring effective single-mode dynamics. To show this, we consider the case of a soliton trap $V_a(\tau) = V_b(\tau)/2 = -(|\beta_{a,2}|/\beta_1\tau_0^2)\text{sech}^2(\tau/\tau_0)$ with width τ_0 , which supports a single bound mode $\Psi_{a,0} = \Psi_{b,0} = (2\tau_0)^{-1/2}\text{sech}(\tau/\tau_0)$. Here, the finite energy gap $\Delta_a = \Delta_b/2 = |\beta_{a,2}|/2\beta_1\tau_0^2$ protects the computational subspace spanned by the bound modes from decoherence; the gap Δ_a corresponds to a phase-mismatch (i.e.,

detuning) between the SH continuum the nonlinear polarization generated by the FH bound mode; similarly, Δ_b corresponds to a phase-mismatch between the FH continuum and the nonlinear polarization generated by the SH bound mode. Taken together, these energy gaps suppress leakage out of the computational subspace by preventing the nonlinear polarization induced by each bound mode from driving continuum modes. For simplicity, we have assumed the dispersion relationships $\beta_{a,2} = \beta_{b,2}/2$ in this work (departure from this condition does not qualitatively change the results). The $\chi^{(2)}$ nonlinear interaction \hat{H}_{NL} between the FH and SH bound modes becomes phase-matched (i.e., resonant) when $\omega_{b,0} - 2\omega_{a,0} = 0$, which can be achieved, e.g., by temperature tuning. As a result, effectively single-mode physics reproducing (2) is realized between the bound FH and SH modes with coupling constant given by $g = \pi r/4\sqrt{2}\tau_0$ (See Appendix D for full discussions). In Fig. 2(a) we show the evolution of a two-photon state instantiated in the FH bound mode, where the photons in the trap are well localized and propagate without dispersing apart from an initial transient. In addition, the dynamics of the SH (Fig. 2(b)) exhibit near-complete Rabi oscillations even for a modest trap with $\Delta/g = 1$, where $\Delta = \Delta_a = \Delta_b/2$ is a characteristic energy gap. These high-contrast Rabi oscillations provide strong evidence of effective single-mode dynamics, which can be further quantified as follows. Ideally, the gate dynamics are confined within the computational subspace spanned by $|20\rangle = 2^{-1/2}(\hat{a}^\dagger)^2|0\rangle$ and $|01\rangle = \hat{b}^\dagger|0\rangle$, so we can directly project the system evolution onto $\text{span}(|20\rangle, |01\rangle)$ in Fig. 2(c). The fact that nearly all of the state amplitude remains in the subspace implies that we have realized the desired single-mode dynamics, i.e., a 180° rotation in the Bloch sphere, picking up a π phase shift after returning to the initial state $|20\rangle$.

Gate fidelity scales favorably even for moderate trap depths. In Fig. 2(d), we plot the error \mathcal{E} of a CZ gate as a function of the gap, where we observe a favorable scaling of $\mathcal{E} \propto (\Delta/g)^{-2}$, which also follows from time-dependent perturbation theory [57]. For a reference input state, we observe that gate operation with fidelity $> 99\%$ is possible with $\Delta/g \gtrsim 3$. To visualize the nature of the gate errors, we also show the temporal distribution of the photons; for a shallow trap, photons leak out as dispersive waves, which effectively act as decoherence channels, and incomplete conversion leads to residual SH power. Deepening the trap increases the confinement to the bound mode, suppressing these dispersive waves. Further, the interaction time $t_\pi \propto \tau_0^{-1/2}$ required to implement the gate also shortens for larger trap depth.

DISPERSION ENGINEERING AND EXPERIMENTAL PROSPECTS

Having established that temporal trapping enables high-fidelity quantum gates with enhanced coupling

rates, we now discuss the prospects for experimental realizations in presently available nanophotonics platforms. In realistic situations, photon loss is the primary decoherence channel for quantum gate operations, and to achieve high gate fidelity the nonlinear coupling rate g has to be larger than the characteristic loss rate κ , which we define as the geometric mean of the FH and SH losses $\kappa = \sqrt{\kappa_a \kappa_b}$. This choice is motivated by analogy to the cooperativity $C \propto g^2/\kappa_{\text{cavity}}\gamma_{\text{atom}}$ in cavity QED systems [58].

For a ring resonator, the nonlinear coupling between the nominal CW modes is

$$g_{\text{cw}} = \frac{v_g \sqrt{\hbar\omega_{b,0}\eta_0}}{\sqrt{T}}, \quad (6)$$

where we have used $r = v_g \sqrt{\hbar\omega_{b,0}\eta_0}$, group velocity v_g , SH frequency $\omega_{b,0}$, and normalized second-harmonic generation (SHG) efficiency η_0 with units $[\text{power}^{-1} \cdot \text{length}^{-2}]$. The round-trip length of the resonator is given by $L = v_g T$, and a smaller L enhances g_{cw} via tighter modal confinement. While microring resonators with radius $\lesssim 100 \mu\text{m}$ have been realized, bending losses make it challenging to significantly reduce the mode volume further, limiting g_{cw} to the order of few megahertz. The same trade-off exists for whispering-gallery-mode resonators (WGMRs). While PhC cavities can realize much smaller wavelength-scale modal confinement and thus a stronger coupling, it is challenging to realize high-Q resonances spanning over an octave, which compromises the overall loss κ and results in g/κ similar in order of magnitude to ring resonators.

In this context, our prescription allows us to circumvent this trade-off between the mode-volume and the loss: the temporal trap forms a smaller “flying cavity” inside a ring resonator, which confines the light further in the axial (temporal) dimension, so that nonlinear interactions between photons benefit from both small mode volume and low loss. Specifically, the nonlinear coupling of the temporally trapped pulses takes the form

$$g_{\text{trap}} = \frac{\pi v_g \sqrt{\hbar\omega_{b,0}\eta_0}}{4\sqrt{2}\tau_0} = \frac{\pi}{4\sqrt{2}} \sqrt{T/\tau_0} g_{\text{cw}}, \quad (7)$$

where the width of the temporal trap τ_0 plays the role of the size of an effective cavity. Comparing g_{trap} to the CW coupling rate of the same resonator, we find that the coupling is enhanced by the factor proportional to the square root of the pulse duty cycle. We note that g_{trap} depends only on τ_0 instead of T , and therefore may realize large coupling rates for resonators of arbitrary length.

For concreteness, in Fig. 3, we show a design of a TFLN resonator optimized for implementing our scheme. This waveguide simultaneously supports a group-velocity matched FH ($\lambda_a = 1560 \text{ nm}$), SH ($\lambda_b = 780 \text{ nm}$), and trap pulse ($\lambda_{\text{trap}} = 2494 \text{ nm}$). The GVD of both of the harmonics are designed to be anomalous, enabling us to create localized bound modes using bright-pulse XPM.

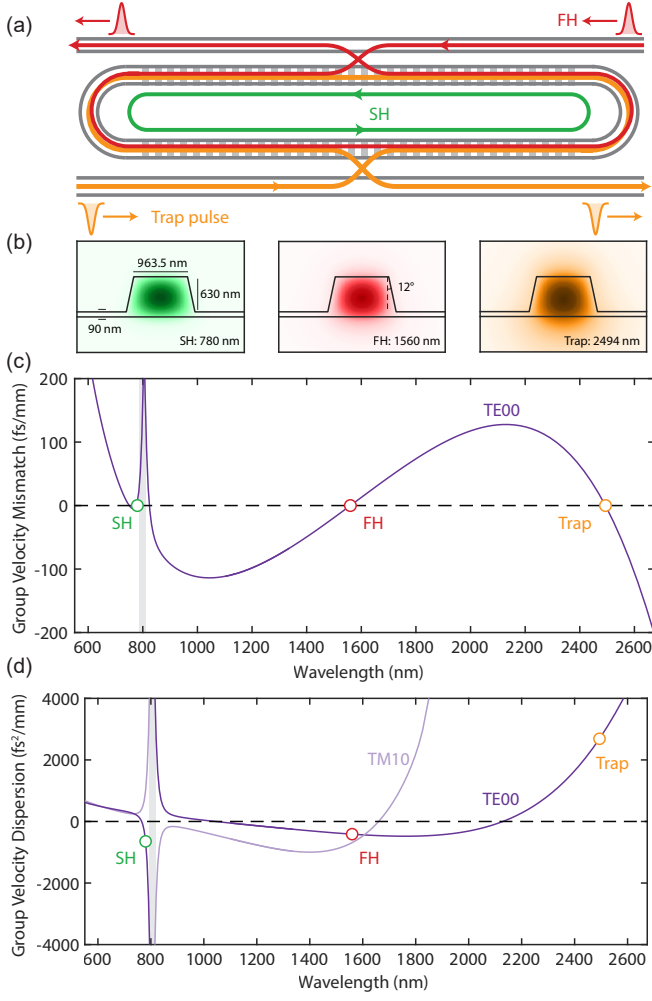


FIG. 3. Design of a microresonator implementing \hat{U}_π with a temporal trap. (a) The FH and trap are coupled into and out of the cavity through two bus waveguides. We assume 100% coupling of the trap pulse, and that FH photons may be switched in and out from the cavity by dynamical coupling [59, 60]. (b) The waveguide geometry and TE00 field distributions associated with each interacting wave; SH (780 nm), FH (1560 nm) and trap pulse (2494 nm), respectively. (c, d) The group velocity mismatch ($\beta_1 - \beta_{1,a}$) and group velocity dispersion (β_2) as a function of wavelength. Shaded grey region: avoided crossing between the TE00 and TM10 modes. With a suitable choice of waveguide geometry we may realize both group velocity matching between the FH and SH, and anomalous dispersion for both harmonics. For the ridge geometries considered here, anomalous dispersion may occur at short wavelengths by choosing the location of the avoided crossing to be red-detuned from the SH.

The minimum trap width τ_0 is limited by the dispersion of the trap pulse, for which we assume $\tau_0 = 50$ fs to ensure the pulse waveform does not disperse over the propagation through the trapping region. With an estimated SHG normalized efficiency of $\eta_0 = 40 \text{ W}^{-1}\text{cm}^{-2}$, we obtain a coupling rate of $g_{\text{trap}}/2\pi = 16.5 \text{ MHz}$. For

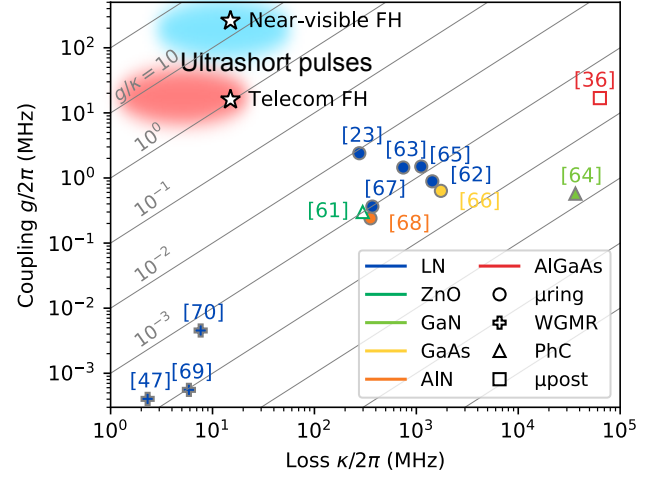


FIG. 4. Figure of merit g/κ shown for various material platforms and geometries, where the filled and the unfilled markers represent experimental and theoretical results, respectively (see Refs. [23, 36, 47, 61–70]). When g is not explicitly characterized, we use experimental measures of $\chi^{(2)}$ nonlinearity, e.g., SHG conversion efficiency, to estimate the coupling (see Appendix E for full discussions). We assume critical coupling, phase-matching between the harmonics, and $\kappa_a = \kappa_b/2$ when the corresponding information is not provided. Stars represent numbers estimated for temporally trapped ultrashort pulses at the telecom ($\lambda_a = 1560$ nm) and the near-visible ($\lambda_a = 800$ nm) FH wavelength.

a 2 mm ring cavity ($T \approx 15$ ps), this is $10\times$ larger than the corresponding g_{cw} obtained without trapping. Moreover, the energy gap of $\Delta/g \approx 100$ provides enough isolation of the trapped modes from the rest of the modes. Regarding the loss, $\alpha = 0.7 \text{ m}^{-1}$ [3 dB/m] has been achieved in TFLN [22], which through the relation $\kappa = \alpha v_g$ corresponds to $\kappa/2\pi = 14.4 \text{ MHz}$. These numbers highlight the potential to reach a near-strong-coupling regime $g/\kappa \geq 1$ using ultrashort pulses with technologies available at present.

Further improvements to g/κ may be possible in next-generation devices by leveraging the scaling of g with both ω and τ_0 , and by improvements to fabrication processes to reach the material-limited loss rates for κ . We note here that (5) is invariant with respect to simultaneous rescalings of β_2 and τ_0^2 ; reductions of the GVD associated with the FH, SH, and trapping pulse enable corresponding reductions of trap pulse duration τ_0 , thereby enhancing g_{trap} . Ultimately, few-cycle operation ($\tau_0 \approx 4\pi/\omega_{\text{trap}}$) may be made possible with new approaches to dispersion engineering that reduce the GVD of the trapping pulse. Short-wavelength operation increases g_{trap} both through the explicit $\omega_{b,0}^{1/2}$ scaling of g_{CW} and the $\eta_0 \sim \omega^4$ [25] scaling associated with the tighter transverse confinement attainable at shorter wavelengths. Recent demonstrations include $\eta_0 = 330 \text{ W}^{-1}\text{cm}^{-2}$ in a TFLN waveguide at $\lambda_b =$

456.5 nm [71], and in principle devices with $\eta_0 > 1000 \text{ W}^{-1}\text{cm}^{-2}$ are possible for FH pulses centered around Ti:sapphire wavelengths. Moreover, the pulse width can be made shorter with a shorter wavelength, i.e., $\tau_0 \sim \omega^{-1}$, amounting to a favorable scaling of $g_{\text{trap}} \sim \omega^3$. Assuming $\lambda_b = 400 \text{ nm}$, which we choose to be below the Urbach tail associated with the material bandgap [72], these scalings anticipate the possibility to achieve $g_{\text{trap}}/2\pi = 260 \text{ MHz}$, corresponding to $g/\kappa > 10$. In addition, process improvements may reduce losses from the present 3–6 dB/m [22, 73] by more than an order of magnitude [45–47], limited primarily by bulk material absorption [48–51, 74]. For known absorption-limited losses of 0.01 m^{-1} , 0.04 m^{-1} , and 1 m^{-1} at 1600, 800, and 400 nm, respectively [74], we find $\kappa/2\pi = 0.4 \text{ MHz}$ for SHG of telecom photons, and $\kappa/2\pi = 4 \text{ MHz}$ for SHG of 800-nm photons. The large coupling rates made possible by temporal trapping, when combined with absorption-limited losses, provide a pathway to $g/\kappa > 40$ at telecom wavelengths and $g/\kappa > 50$ at visible wavelengths. We compare these numbers against the current state of the art in a variety of material systems and waveguide geometries in Fig. 4. To date, the highest recorded g/κ based on optical nonlinearities is $g/\kappa \approx 10^{-2}$ in a 1560-nm pumped TFLN microresonator [75]. In principle, short-wavelength operation and reductions in resonator loss may push conventional CW-pumped nonlinear devices toward $g/\kappa = 0.1$ – 1 . In contrast, the g/κ enabled by nonlinear resonators using temporal trapping may exceed these limits by two orders of magnitude.

CONCLUSION

In this work, we show that temporally trapping ultrashort pulses can realize strong photon-photon interactions by simultaneously leveraging both temporal and spatial field confinement. The energy gap created between the trapped mode and the rest of the cavity modes suppresses undesired multimode interactions, realizing effective single-mode dynamics necessary for high-fidelity quantum gate operations. Our full-quantum simulations confirm that coherent nonlinear dynamics of temporally trapped ultrashort pulses can realize high-fidelity two-qubit entangling gates in a deterministic manner. This resolves the longstanding concern first raised by Shapiro that pulsed nonlinear optics cannot

implement high-fidelity quantum gates [26, 27].

Temporal trapping significantly brightens the prospects of achieving strong coupling in existing photonic platforms [76, 77]. By reducing the effective cavity volume by the pulse duty cycle, g/κ can be increased by over an order of magnitude. Notably, numerical modeling based on realistic dispersion-engineered waveguide designs shows that $g/\kappa \sim 1$ is possible on existing TFLN platforms, and true strong coupling $g/\kappa \gg 1$ is plausible with realistic assumptions on wavelength scaling and loss, proposing a unique route towards deterministic optical quantum computation using ultrashort pulses.

Our generic prescription of using temporal trapping to realize enhanced single-mode nonlinear coupling can, in principle, be applied to a broad range of scenarios beyond discrete-variable NLOQC. For example, continuous-variable implementations of optical quantum computing [78, 79] suffer from the same tradeoff between linearity and determinism. Applied to these systems, strong coupling in a $\chi^{(2)}$ cavity can enable deterministic non-Gaussian gate operations and resource state preparations [56, 80, 81], circumventing the need for probabilistic implementations using measurement and feedback [82, 83]. Combined with the ability to manipulate temporal mode structures with optical pulse gating [84, 85], deterministic quantum operations on arbitrary photon temporal modes could be realized. Our scheme is compatible with intracavity time-multiplexing [28, 86] and traveling-wave implementations, enabling unprecedented scalability, qubit uniformity, and operation bandwidth. We expect our work to shed light on the potential to harness ultrafast pulse dynamics for coherent quantum computation and engineering, guiding ongoing experimental and theoretical efforts towards this unique frontier of broadband quantum optics.

ACKNOWLEDGEMENTS

This work has been supported by the Army Research Office under Grant No. W911NF-16-1-0086, and the National Science Foundation under awards CCF-1918549 and PHY-2011363. The authors wish to thank NTT Research for their financial and technical support. R. Y. is supported by a Stanford Q-FARM Ph.D. Fellowship and the Masason Foundation.

APPENDIX A: NONLINEAR HAMILTONIAN

1. Generic Form

This section derives the general Hamiltonian for a nonlinear-optical cavity. A fully rigorous derivation is very involved, as one must account for dispersion in the linear and nonlinear polarizabilities, and take care to properly quantize fluctuations using the D field [87–89]. However, for weakly dispersive materials and perturbative nonlinearities, a simpler phenomenological model suffices [90]. To start, assume a wavelength-independent refractive

index. We write the electric field as a sum of normal-mode fluctuations

$$E(\vec{x}, t) = \sum_m \sqrt{\hbar\omega_m/2\epsilon_0} (A_m(t)E_m(\vec{x}) + \text{c.c.}), \quad (\text{A1})$$

where the $E_m(\vec{x})$ are normalized to $\int n(\vec{x})^2 |E_m(\vec{x})|^2 d^3x = 1$. We first solve Eq. (A1) by treating $A_m(t)$ as classical variables, which must evolve to satisfy the Helmholtz equation:

$$\nabla \times (\nabla \times E) + \frac{n^2}{c^2} \frac{\partial^2 E}{\partial t^2} = -\frac{1}{c^2} \frac{\partial^2 (\delta P/\epsilon_0)}{\partial t^2} \quad (\text{A2})$$

In the absence of a perturbing term δP , $\dot{A}_m = -i\omega_m A_m$, since the E_m are normal modes. Linear perturbations $\delta P/\epsilon_0 = \delta\epsilon_r E$ alter the mode frequencies via the well-known expression $\delta\omega_m = -\frac{1}{2}\omega_m \int \delta\epsilon_r |E_m|^2 d^3\vec{x}$ [91]. This expression can be generalized to [90]:

$$\delta\dot{A}_m = \frac{i\omega_m}{2\sqrt{\hbar\omega_m/2\epsilon_0}} \int E_m^* \delta P d^3\vec{x} \quad (\text{A3})$$

2. Parametric ($\chi^{(2)}$) Material

For the parametric nonlinearity, $\delta P_i = \frac{1}{2}d_{ijk}E_jE_k \equiv \frac{1}{2}d : EE$. The resulting equation of motion, simplified using Kleinman symmetry [92] is:

$$\begin{aligned} \dot{A}_m &= -i\omega_m A_m + i \sum_{np} \sqrt{\frac{\hbar\omega_m\omega_n\omega_p}{2\epsilon_0}} \left[A_n A_p \int_* d : E_m^* E_n E_p d^3\vec{x} + 2A_n^* A_p \int_* d : E_m^* E_n^* E_p d^3\vec{x} \right] \\ &= -i\omega_m A_m + \frac{i}{2} \sum_{np} (g_{m,np} A_n A_p + g_{p,mn}^* A_n^* A_p), \quad g_{m,np} \equiv \sqrt{\frac{2\hbar\omega_m\omega_n\omega_p}{\epsilon_0}} \int_* d : E_m^* E_n E_p d^3\vec{x} \end{aligned} \quad (\text{A4})$$

(Here $\int_* (\dots) d^3\vec{x}$ refers to an integral restricted to the nonlinear material.) Now we quantize the fields, replacing $A_m \rightarrow \hat{A}_m$ with canonical commutators $[\hat{A}_m, \hat{A}_n] = 0$, $[\hat{A}_m, \hat{A}_n^\dagger] = \delta_{mn}$. Eq. (A4) is generated by the following Hamiltonian:

$$\hat{H} = \sum_m \omega_m \hat{A}_m^\dagger \hat{A}_m - \frac{1}{2} \sum_{mnp} (g_{m,np} \hat{A}_m^\dagger \hat{A}_n \hat{A}_p + \text{h.c.}) \quad (\text{A5})$$

The simplest case involves a two-mode cavity where FH \hat{a} and SH \hat{b} . Here, up to a phase, $\hat{H}_{\text{NL}} = \frac{1}{2}g(a^2 b^\dagger + (a^\dagger)^2 b)$, where g is given by:

$$g \equiv g_{b,aa} = \sqrt{\frac{4\hbar\omega^3}{\epsilon_0}} \int_* d : E_b^* E_a E_a d^3\vec{x} \quad (\text{A6})$$

Here, as before, we have energy-normalized the modes as $\int \epsilon_r |E|^2 d^3\vec{x} = 1$.

Two related quantities are often used to quantify the nonlinear interaction: the effective mode volume V_{sh} (usually normalized as $\tilde{V}_{\text{sh}} = V_{\text{sh}}/(\lambda/n)^3$) and the nonlinear overlap $\bar{\beta}$:

$$\tilde{V}_{\text{sh}} = \left| \int_* \hat{d} : E_b^* E_a E_a d^3\vec{x} \right|^{-2}, \quad \bar{\beta} = \lambda^{3/2} \int_* \hat{d} : E_b^* E_a E_a d^3\vec{x} = \frac{1}{\sqrt{n^3 \tilde{V}_{\text{sh}}}} \quad (\text{A7})$$

Here, $\hat{d}_{ijk} = d_{ijk}/d_{\text{eff}}$ is the normalized nonlinear tensor. The volume is defined relative to an “ideal” cavity: for hypothetical flat-top modes with constant norm $|E_a|, |E_b| = \text{const}$ and perfect phase-matching, V_{sh} will return the physical cavity volume. Note, however, that poor mode overlap can cause \tilde{V}_{sh} to be much larger than the actual volume of either mode.

Relative to these quantities, g is given by:

$$g = \frac{4d_{\text{eff}}}{\lambda^3} \sqrt{\frac{2\pi^3 \hbar c^3}{n^3 \epsilon_0 \tilde{V}_{\text{sh}}}} = \frac{4d_{\text{eff}} \bar{\beta}}{\lambda^3} \sqrt{\frac{2\pi^3 \hbar c^3}{\epsilon_0}} \quad (\text{A8})$$

The effective loss rate is $\kappa \equiv \sqrt{\kappa_a \kappa_b} = (2\pi c/\lambda) \sqrt{2/Q_a Q_b}$. Dividing these quantities yields the expression for g/κ , Eq. (3). For LiNbO₃ at $\lambda = 1.55 \mu\text{m}$ ($n = 2.2$, $d_{33} = 33 \text{ pm/V}$), this expression yields $g/\kappa \approx 10^{-6} \sqrt{Q_a Q_b / \tilde{V}_{\text{sh}}}$.

	Q_a	Q_b	\tilde{V}_k	\tilde{V}_{sh}	d_{eff}/d_{33}	$C_{\chi^{(2)}}$	$C_{\chi^{(3)}}$
PhC*	10^6	10^3	10^{-2}	1	1	0.03	0.02
Ring†	10^7	10^7	2000	2000	$2/\pi$	0.1	$\sim 10^{-6}$
Trapped‡	10^7	10^7	20	20	$2/\pi$	1	$\sim 10^{-3}$

TABLE II. Estimates of Q , V , and cooperativity ($C_{\chi^{(2)}} = g/\kappa$, $C_{\chi^{(3)}} = \chi/\kappa$) for competing confinement mechanisms, Si and LiNbO₃, $\lambda = 1.55 \mu\text{m}$. *Tip-cavity PhC engineered to have a deep-subwavelength volume [93, 94]. †Ring circumference 2 mm, loss $\alpha = 3 \text{ dB/m}$ [22]. ‡Pulse of width 50 fs, loss $\alpha = 3 \text{ dB/m}$.

3. Kerr ($\chi^{(3)}$) Material

For comparison, we also provide estimates for the nonlinear coupling in a Kerr material. Here, the nonlinear polarization $P_{\text{NL}}/\epsilon_0 = \chi : EEE$ is cubic in E . Applying Eq. (A3) and ignoring the off-resonant third-harmonic terms, we find:

$$\dot{A}_m = -i\omega_m A_m + i \sum_{npq} \chi_{mn,pq} A_n^* A_p A_q, \quad \chi_{mn,pq} = \frac{3\hbar\sqrt{\omega_m\omega_n\omega_p\omega_q}}{4\epsilon_0} \int_* \chi : E_m^* E_n^* E_p E_q d^3\vec{x} \quad (\text{A9})$$

Upon quantizing the fields, this corresponds to the Hamiltonian:

$$\hat{H} = \sum_m \omega_m \hat{A}_m^\dagger \hat{A}_m - \frac{1}{2} \sum_{mn,pq} \chi_{mn,pq} \hat{A}_m^\dagger \hat{A}_n^\dagger \hat{A}_p \hat{A}_q \quad (\text{A10})$$

Reducing this to a singly-resonant cavity with field \hat{a} , we obtain $\hat{H} = \omega \hat{a}^\dagger \hat{a} - \frac{1}{2} \chi \hat{a}^\dagger \hat{a}^\dagger \hat{a} \hat{a}$, where

$$\chi = -\frac{3\hbar\omega^2}{4\epsilon_0} \int_* \chi : E^* E^* E E d^3\vec{x} = \frac{3\pi^2 \hbar c^2 \chi_{\text{eff}}}{n\epsilon_0 \lambda^5 \tilde{V}_{rmk}}, \quad V_k = \left(n^4 \int_* \hat{\chi} : E^* E^* E E d^3\vec{x} \right)^{-1} \quad (\text{A11})$$

Here, as before, $\hat{\chi} = \chi/\chi_{\text{eff}}$ is the normalized Kerr tensor. Given $\kappa = 2\pi c/\lambda Q$, the figure of merit for the Kerr cavity is:

$$\frac{\chi}{\kappa} = \frac{3\pi \hbar c \chi_{\text{eff}}}{2n\epsilon_0 \lambda^4} \frac{Q_a}{\tilde{V}_k} \quad (\text{A12})$$

For silicon at $1.55 \mu\text{m}$ ($n = 3.5$, $\chi = 0.3 \text{ nm}^2/\text{V}^2$), $\chi/\kappa \approx (2 \times 10^{-10}) Q_a/\tilde{V}_k$. Table II compares the cooperativity of $\chi^{(2)}$ and $\chi^{(3)}$ mechanisms for the PhC, ring, and trapped-pulse situations.

APPENDIX B: RING CAVITY AND NORMALIZATION

1. Ring Cavity

Ring cavities enjoy cylindrical symmetry, so the eigenmodes, which can be found with separation of variables, integer angular quantum number (i.e. dependence $E_m \sim e^{im\phi}$). Most rings are large enough that they can be modeled as waveguides that “wrap around” at length $L = 2\pi R$; in this case, the axial variable is $z \equiv R\phi$ and the transverse variables are $x \equiv \rho - R$ and y . The modes $E_{m,n}(\vec{x}) = L^{-1/2} E_{m,n}^\perp(x, y) e^{2\pi i m z/L}$ are indexed by axial and transverse quantum numbers (m, n). Due to phase-matching conditions, only a single transverse mode participates meaningfully in the dynamics, so to simplify the notation, we drop the transverse index n and the superscript \perp when writing E : $E_{m,n}^\perp(x, y) \rightarrow E_m(x, y)$.

The Hamiltonian takes the form of Eq. (A5), where the coupling elements are given by:

$$g_{m,np} = \sqrt{\frac{2\hbar\omega_m\omega_n\omega_p}{\epsilon_0 L}} \tilde{\pi}_{m-n-p} \int_* d : E_m^* E_n E_p dA \quad (\text{B1})$$

where the $\tilde{\pi}_m$ are the Fourier series coefficients of the poling function $\pi(z) : [0, L] \rightarrow \{-1, +1\}$, defined as $\tilde{\pi}_m = L^{-1} \int \pi(z) \cos(2\pi m z/L) dz$. For modal phase-matching, $\pi(z) = 1$ and $\tilde{\pi}_m = \delta_{m0}$. For quasi-phase matching with 50%

duty cycle, $\pi(z) = \text{sign}(\cos(2\pi sz/L))$, where $s \in \mathbb{Z}$ is the number of poling periods per circumference. The QPM factor works out to $\tilde{\pi}_{\pm s} = 2/\pi$ (higher-order QPM processes are not relevant here).

Since the trapped pulses comprise many optical cycles, their bandwidth is narrow compared to the carrier frequency. In this case, we can use a two-band model that separates the FH (a_m) and SH (b_m), depicted in Fig. 5:

$$\begin{cases} \hat{a}_m = \hat{A}_{m_a+m}, & \hat{b}_m = \hat{A}_{m_b+m} \\ \omega_{a,m} = \omega_{m_a+m}, & \omega_{b,m} = \omega_{m_b+m} \end{cases} \quad (\text{B2})$$

In the two-band model, the pulses are narrow-band enough that the cross-sectional fields $E_{a,m} \equiv E_{m+m_a}$, $E_{b,m} \equiv E_{m+m_b}$ depend only weakly on index m ; we can therefore suppress the index $E_{a,m} \rightarrow E_a$, $E_{b,m} \rightarrow E_b$. The cavity is poled to phase-match \hat{a}_0 and \hat{b}_0 , i.e. $s = m_b - 2m_a$. Under these assumptions, the Hamiltonian Eq. (A5) reduces to:

$$H = \sum_m (\omega_{a,m} \hat{a}_m^\dagger \hat{a}_m + \omega_{b,m} \hat{b}_m^\dagger \hat{b}_m) - \frac{r}{2\sqrt{T}} \sum_{mn} (\hat{b}_{m+n}^\dagger \hat{a}_m \hat{a}_n + \hat{b}_{m+n} \hat{a}_m^\dagger \hat{a}_n^\dagger) \quad (\text{B3})$$

where $T = n_g L/c$ is the cavity repetition rate at a designated group velocity c/n_g (defined below), and

$$r = 2d_{\text{eff}} \sqrt{\frac{\hbar \omega^3 n_g}{\epsilon_0 c}} \int_* \hat{d} : E_b^* E_a E_a dA = \frac{4d_{\text{eff}}}{n^2} \sqrt{\frac{2\pi^3 n_g \hbar c^2}{\epsilon_0 \lambda^5 \tilde{A}_{\text{sh}}}} \quad (\text{B4})$$

is the parametric interaction strength. As in Sec. A 2, we define an effective mode area $A_{\text{sh}} = |n^3 \int_* \hat{d} : E_b^* E_a E_a dA|^{-2}$, where $\tilde{A}_{\text{sh}} = A_{\text{sh}}/(\lambda/n)^2 \sim 1$ for high-index-contrast waveguides. We can relate r to the normalized SHG efficiency η_0 , a value experimentally quoted for waveguides [71, 95–97], as follows:

$$r = \sqrt{\frac{4\pi c^3 \hbar \eta_0}{\lambda n_g^2}} = v_g \sqrt{2\hbar \omega \eta_0}, \quad \eta \equiv \frac{8\pi^2 Z_0 n_g^3 d_{\text{eff}}^2}{\lambda^2} \left| \int_* \hat{d} : E_b^* E_a E_a dA \right|^{-2} = \frac{8\pi^2 Z_0 n_g^3 d_{\text{eff}}^2}{\lambda^4 n^4 \tilde{A}_{\text{sh}}} \quad (\text{B5})$$

We perform a rotating-wave transformation to move into the co-propagating basis with designated carrier frequency ω and repetition rate Ω (which corresponds to group index $n_g = 2\pi c/L\Omega$): $\hat{a}_m \rightarrow e^{-i(\omega+m\Omega)t} \hat{a}_m$, $\hat{b}_m \rightarrow e^{-i(2\omega+m\Omega)t} \hat{b}_m$. The effect of this transformation is to shift the energy levels $\omega_{a,m}, \omega_{b,m}$:

$$\omega_{a,m} \rightarrow \omega_{a,m} - (\omega + \Omega t), \quad \omega_{b,m} \rightarrow \omega_{b,m} - (2\omega + \Omega t) \quad (\text{B6})$$

In the dispersion-engineered case, the FH and SH pulses travel at nearly-matched group velocities $n_{a,g} \approx n_{b,g} \approx n_g$ and T is chosen as a corresponding average round-trip time. Specifically, for a given $n_g = cT/L$, define $\Delta n_{u,g} = n_{u,g} - n_g$. Up to quadratic order in dispersion, the resonance frequencies in the rotating frame are:

$$\omega_{u,m} = \omega_{u,0} - \frac{\Delta n_{u,g}}{n_g^2} \Omega m + \frac{\beta_{u,2} c}{2n_g} \Omega^2 m^2 \quad (\text{B7})$$

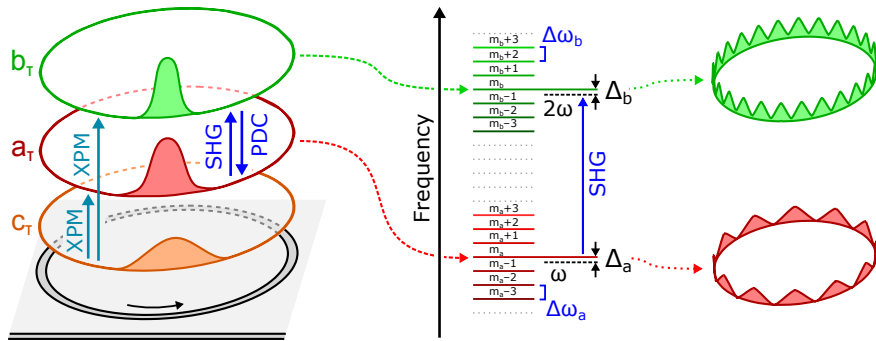


FIG. 5. Pulses propagating along the ring resonator in the two-band model. Spectrum is divided into FH \hat{a}_m and SH \hat{b}_m modes, while the trap field is nonresonant.

Finally, we perform a Fourier transform to convert the propagating fields \hat{a}_m, \hat{b}_m into a temporal basis, depending on the “fast time” τ :

$$a(t, \tau) = \frac{1}{\sqrt{T}} \sum_m a_m(t) e^{2\pi i m \tau / T}, \quad b(t, \tau) = \frac{1}{\sqrt{T}} \sum_m b_m(t) e^{2\pi i m \tau / T} \quad (\text{B8})$$

These fields are normalized so that $[a(t, \tau), a^\dagger(t, \tau')] = \delta(\tau - \tau')$, etc., and are periodic in τ . In the group-velocity matched case $\Delta n_{u,g} = 0$, the resulting Hamiltonian is:

$$\hat{H} = \frac{r}{2} \int d\tau \left(\hat{a}_\tau^{\dagger 2} \hat{b}_\tau + \hat{a}_\tau^2 \hat{b}_\tau^\dagger \right) + \sum_{u \in \{a,b\}} \int d\tau \hat{u}_\tau^\dagger \left(\omega_{u,0} + \frac{\beta_{u,2}}{2\beta_1} \partial_\tau^2 \right) \hat{u}_\tau, \quad (\text{B9})$$

Finally, we introduce the trapping field. This field is not resonant with the cavity, so it can be treated as an external τ -dependent potential term in the Hamiltonian. This yields the final form of the Hamiltonian, which is given in Eq. (4):

$$\hat{H} = \frac{r}{2} \int d\tau \left(\hat{a}_\tau^{\dagger 2} \hat{b}_\tau + \hat{a}_\tau^2 \hat{b}_\tau^\dagger \right) + \sum_{u \in \{a,b\}} \int d\tau \hat{u}_\tau^\dagger \left(\omega_{u,0} + \frac{\beta_{u,2}}{2\beta_1} \partial_\tau^2 + V_u(\tau) \right) \hat{u}_\tau, \quad (\text{B10})$$

where $V_b(\tau) = 2V_a(\tau)$.

2. Normalization

In this section, we describe how we transform the dimensionful Hamiltonian Eq. (B10) of the $\chi^{(2)}$ -nonlinear waveguide into a dimensionless form well suited for numerical simulation. Furthermore, nondimensionalization also allows us to extract essential dimensionless parameters which uniquely characterize the system dynamics. For simplicity, we assume here that both harmonics have equal group velocities and anomalous group velocity dispersions, but the following can readily be extended to handle more general cases.

First, we introduce characteristic fast and slow timescales $t_c = (|\beta_{a,2}|/r^4\beta_1)^{1/3}$ and $\tau_c = (|\beta_{a,2}|/r\beta_1)^{2/3}$, respectively. This allows us to rewrite the Hamiltonian as

$$\hat{H} = \frac{1}{t_c} \left\{ \frac{1}{2} \int d\xi \left(\hat{a}_\xi^{\dagger 2} \hat{b}_\xi + \hat{a}_\xi^2 \hat{b}_\xi^\dagger \right) + \int d\xi \hat{a}_\xi^\dagger \left(-\frac{1}{2} \partial_\xi^2 + \omega_{a,0} t_c + U(\xi) \right) \hat{a}_\xi + \int d\xi \hat{b}_\xi^\dagger \left(-\frac{\rho}{2} \partial_\xi^2 + \omega_{b,0} t_c + 2U(\xi) \right) \hat{b}_\xi \right\}, \quad (\text{B11})$$

where $\xi = \tau/\tau_c$ is the normalized (dimensionless) fast-time coordinate, $\rho = \beta_{b,2}/\beta_{a,2}$ is the ratio between the SH and FH GVDs, and $U(\xi) = V_a(\xi\tau_c)t_c = \frac{1}{2}V_b(\xi\tau_c)t_c$ is the normalized potential. Note that these specific choices of t_c and τ_c fix the coefficients for the nonlinear coupling and the FH GVD to a canonical value of 1/2.

Next, we move to a rotating frame of the FH via the operator mappings $\hat{a} \mapsto e^{-i\omega_{a,0}t} \hat{a}$ and $\hat{b} \mapsto e^{-2i\omega_{a,0}t} \hat{b}$, after which we obtain

$$\hat{H} = \frac{1}{t_c} \left\{ \frac{1}{2} \int d\xi \left(\hat{a}_\xi^{\dagger 2} \hat{b}_\xi + \hat{a}_\xi^2 \hat{b}_\xi^\dagger \right) + \int d\xi \hat{a}_\xi^\dagger \left(-\frac{1}{2} \partial_\xi^2 + U(\xi) \right) \hat{a}_\xi + \int d\xi \hat{b}_\xi^\dagger \left(\delta - \frac{\rho}{2} \partial_\xi^2 + 2U(\xi) \right) \hat{b}_\xi \right\}, \quad (\text{B12})$$

where we have introduced the normalized phase mismatch $\delta = (\omega_{b,0} - 2\omega_{a,0})t_c$. At this point, we note that (B12) has only three dimensionless quantities that nontrivially determine the system dynamics, i.e., U , δ , and ρ . As a result, two systems with identical U , δ , and ρ after normalization exhibit quantum dynamics that are equivalent up to simple rescalings of the two time coordinates.

As a further simplification, we consider in the main text a sech-shaped trap $V_a(\tau) = V_b(\tau)/2 = -(|\beta_{a,2}|/\beta_1\tau_0^2) \text{sech}^2(\tau/\tau_0)$ with zero phase-mismatch $\omega_{b,0} - 2\omega_{a,0} = 0$ and $\beta_{a,2} = \beta_{b,2}/2$, which in dimensionless form corresponds to $U(\xi) = -\xi_0^{-2} \text{sech}^2(\xi/\xi_0)$, $\delta = 0$, and $\rho = 2$. As a result, the normalized trap width $\xi_0 = \tau_0/\tau_c$ is left as the sole parameter which uniquely determines the system dynamics. In particular, ξ_0 determines the ratio between the characteristic energy gap $\Delta = \Delta_a$ and the nonlinear coupling between the bound mode g via the reciprocal relationship

$$\frac{\Delta}{g} = \frac{2\sqrt{2}}{\pi} \xi_0^{-3/2}, \quad (\text{B13})$$

which indicates that we can also equivalently use Δ/g to uniquely characterize the system dynamics.

APPENDIX C: NUMERICAL SIMULATION OF THE QUANTUM PULSE PROPAGATION

In general, full quantum simulations of the pulse propagation dynamics can be readily performed by leveraging techniques such as matrix product states [98] or supermode expansion [99], especially when written in the dimensionless form introduced in Appendix B.

However, in this work, we are primarily concerned with quantum pulses containing only up to two FH or one SH photons, which can be more directly and concisely captured using a wavefunction of the general form

$$|\varphi(t/t_c)\rangle = \left(P + \int d\xi Q_\xi \hat{a}_\xi^\dagger + \int d\xi_1 d\xi_2 R_{\xi_1, \xi_2} \hat{a}_{\xi_1}^\dagger \hat{a}_{\xi_2}^\dagger + \int d\xi S_\xi \hat{b}_\xi^\dagger \right) |0\rangle. \quad (C1)$$

The time evolution of the wavefunction under (B12) can then be shown to obey $\frac{\partial P}{\partial(t/t_c)} = 0$ and

$$\begin{aligned} i \frac{\partial Q_\xi}{\partial(t/t_c)} &= \left(-\frac{1}{2} \partial_\xi^2 + U(\xi) \right) Q_\xi \\ i \frac{\partial S_\xi}{\partial(t/t_c)} &= \left(\delta - \frac{\rho}{2} \partial_\xi^2 + 2U(\xi) \right) S_\xi + R_{\xi, \xi}(t) \\ i \frac{\partial R_{\xi_1, \xi_2}}{\partial(t/t_c)} &= \left(-\frac{1}{2} (\partial_{\xi_1}^2 + \partial_{\xi_2}^2) + U(\xi_1) + U(\xi_2) \right) R_{\xi_1, \xi_2} + \frac{1}{2} \delta(\xi_1 - \xi_2) S_{\xi_1}, \end{aligned} \quad (C2)$$

which can be efficiently integrated, e.g., by split-step Fourier methods.

APPENDIX D: TEMPORAL SUPERMODES FOR PULSED QUANTUM GATE OPERATIONS

In discussing quantum gate operations with photonic qubits, it is often implicitly assumed that the computational mode of the qubit is static and well defined for all time, and this is often the case in single-mode quantum systems such as microring resonators or photonic crystal cavities. For a multimode pulsed system, however, computational modes can take the form of any collective excitation $\int d\tau \Psi(\tau) \hat{a}_\tau$, so a complete description of a quantum gate must include not only the gate Hamiltonian but also the specification of both the input and output computational modes, $\hat{a}_{\text{in/out}} = \int d\tau \Psi_{\text{in/out}}^*(\tau) \hat{a}_\tau$. In the presence of dispersion, we generically require $\hat{a}_{\text{out}} \neq \hat{a}_{\text{in}}$ even for a linear gate operation, and failure to choose an appropriate mode for the output can lead to loss of photons and hence fidelity. Of course, for a linear gate operation, one can always compute the correct output mode given the input mode using a linear scattering formalism, but this approach does not work for a nonlinear gate governed by a nonlinear multimode Hamiltonian. In this latter case, the problem devolves into numerical optimization of the input and output waveforms $\Psi_{\text{in/out}}(\tau)$, and even then, it is not guaranteed that there exists any input/output mode pair which allows for unit gate fidelity.

For the Kerr-phase gate, the intended action of the gate can be explicitly written in terms of photons in the input and output modes as

$$\hat{U}_\pi [c_0 |0_{\text{in}}\rangle + c_1 |1_{\text{in}}\rangle + c_2 |2_{\text{in}}\rangle] = c_0 |0_{\text{out}}\rangle + c_1 |1_{\text{out}}\rangle - c_2 |2_{\text{out}}\rangle, \quad (D1)$$

where $|n_{\text{in/out}}\rangle = \frac{1}{\sqrt{n!}} \hat{a}_{\text{in/out}}^{\dagger n}(t) |0\rangle$ is the n -photon Fock state of the input/output mode. We also denote signal waveforms at intermediate times as $\Psi_a(\tau, t)$, so, for example, we have $\Psi_{\text{in}}(\tau) = \Psi_a(\tau, 0)$ and $\Psi_{\text{out}}(\tau) = \Psi_a(\tau, t_\pi)$. Here, our aim is, by choosing appropriate input/output waveforms, to implement \hat{U}_π as faithfully as possible given the fixed action of the waveguide $e^{-i\hat{H}t_\pi}$. For this purpose, a reasonable approach would be to ensure at least perfect gate operation on the single-photon input, i.e., to fix the output mode according to

$$|1_{\text{out}}\rangle = e^{-i\hat{H}t_\pi} |1_{\text{in}}\rangle, \quad (D2)$$

which can be realized when $\Psi_a(\tau, t)$ is taken as the solution to

$$i\partial_t \Psi_a = \hat{G}_a \Psi_a. \quad (D3)$$

In this case, since the vacuum part evolves trivially, the only possible source of gate error is the action of $e^{-i\hat{H}t_\pi}$ on the two-photon part $|2_{\text{in}}\rangle$, which can be characterized, e.g., by an error measure $\mathcal{D} = \|\psi_{\text{out}}\rangle + |2_{\text{out}}\rangle\| = \sqrt{2(1 + \text{Re} \langle \psi_{\text{out}} | 2_{\text{out}} \rangle)}$ with $|\psi_{\text{out}}\rangle = e^{-i\hat{H}t_\pi} |2_{\text{in}}\rangle$.

A natural way to fulfill (D3) is to set the input (and output) waveform to be an eigenmode of $\hat{G}^{(a)}$. In the absence of a temporal trap, however, these eigenmodes correspond to monochromatic cavity modes with weak nonlinearity due to their large mode volumes. Thus, we are motivated to consider nonstationary, pulsed solutions to (D3) in order to increase the nonlinear coupling. To be concrete, we consider Gaussian waveforms which solve (D3) as $\Psi_a(\tau, t) = e^{-i\omega_{a,0}t} \Psi_g(\tau, t - t_g)$ with

$$\Psi_g(\tau, t - t_g) = \pi^{-1/4} \sqrt{\frac{\tau_g/\tau_c}{\tau_g^2/\tau_c^2 + i(t - t_g)/t_c}} \exp\left(-\frac{\tau^2/\tau_c^2}{2(\tau_g^2/\tau_c^2 + i(t - t_g)/t_c)}\right). \quad (\text{D4})$$

Here, τ_g is the pulse width, and t_g characterizes the initial chirp, which we set to $t_g = t_\pi/2$ to minimize the maximum chirp during the gate operation. Where needed in the main text, we can similarly take the corresponding SH mode to be $\Psi_b(\tau, t) = e^{-i\omega_{b,0}t} \Psi_g(\tau, \rho(t - t_g))$ with $\rho = \beta_{b,2}/\beta_{a,2}$.

As described above, the gate error of this pulsed Kerr-phase gate is limited by its error acting on $|2_{\text{in}}\rangle$. Therefore, we present in Fig. 6 the error \mathcal{D} for the input state $|2_{\text{in}}\rangle$ as a function of the gate time t_π and pulse width τ_g . While we do observe a slow improvement of the gate performance at longer gate times, perfect gate operation appears far from achievable. These gate errors are induced by undesired multimode nonlinear interactions with orthogonal modes, underscoring the challenges inherent to a traveling-pulse implementation of a nonlinear quantum gate. It is also worth mentioning that there exists a trade-off between the maximum temporal confinement and the rate of pulse dispersion in (D4) (i.e., pulses with smaller width disperse faster), making it difficult to simultaneously achieve large temporal confinement and long interaction time.

On the other hand, in the presence of a temporal trap, we can take Ψ_a to be a localized (bound) eigenmode of \hat{G}_a , which naturally leverages temporal confinement to enhance the nonlinear coupling. To see that this choice of Ψ_a can realize effective single-mode dynamics and high-fidelity gate operations, let us consider the set of eigenmodes given by (for $u \in \{a, b\}$)

$$\hat{u}_m(t) = \int d\tau e^{i\lambda_{u,m}t} \Psi_{u,m}^*(\tau) \hat{u}_\tau, \quad (\text{D5})$$

where $\lambda_{u,m}$ and $\Psi_{u,m}(\tau)$ are the eigenvalue and the eigenmode of (5), respectively. The Hamiltonian (4) rewritten in terms of these eigenmodes is

$$\hat{H} = \sum_{\ell mn} \frac{g_{\ell mn}}{2} e^{i\delta_{\ell mn}t} \hat{a}_m^\dagger(t) \hat{a}_n^\dagger(t) \hat{b}_\ell(t) + \text{H.c.} \quad (\text{D6})$$

with a nonlinear coupling tensor

$$g_{\ell mn} = r \int d\tau \Psi_{b,\ell}^*(\tau) \Psi_{a,m}(\tau) \Psi_{a,n}(\tau) \quad (\text{D7})$$

and a phase-mismatch tensor

$$\delta_{\ell mn} = \lambda_{b,n} - \lambda_{a,\ell} - \lambda_{a,m}. \quad (\text{D8})$$

In the presence of a deep enough trap, we can realize $|\delta_{\ell mn}/g_{\ell mn}| \gg 1$, which strongly suppresses the nonlinear coupling unless special care is taken to make the process resonant.

Specifically, with a temporal trap of the form $V_a(\tau) = V_b(\tau)/2 = -(|\beta_{a,2}|/\beta_1\tau_0^2)\text{sech}^2(\tau/\tau_0)$ and $\rho = 2$ considered in the main text, we have $\Psi_{a,0} = \Psi_{b,0} = (2\tau_0)^{-1/2} \text{sech}(\tau/\tau_0)$ with a characteristic energy gap of $\Delta = \Delta_a = |\beta_{a,2}|/2\beta_1\tau_0^2$. By setting $\omega_{b,0} - 2\omega_{a,0} = 0$, we can set $\delta_{000} = 0$ which brings the nonlinear interaction between fundamental eigenmodes (i.e., between the computational modes) to resonance. At the same time, leakage of photons from the computational modes are mediated by couplings of the form $g_{\ell 00}$ and g_{0mn} , and it can be shown that $|\delta_{\ell 00}|$ and $|\delta_{0mn}|$ are lower bounded by Δ , thus suppressing leakage when Δ is large. As a result, photons are confined in the fundamental supermodes, where they experience single-mode dynamics described by an effective Hamiltonian

$$\hat{H} \approx \frac{g}{2} (\hat{a}^2 \hat{b}^\dagger + \hat{a}^{\dagger 2} \hat{b}), \quad (\text{D9})$$

where we identify $g = g_{000} = \pi r/4\sqrt{2\tau_0}$, $\hat{a} = \hat{a}_0$, and $\hat{b} = \hat{b}_0$. As shown in the main text, the quantum dynamics under (D9) can be used to implement a high-fidelity Kerr-phase gate.

The emergence of the single-mode dynamics in the presence of a temporal trap is a generic phenomena and does not depend on the particular shape of the potential. For instance, under a more generic potential $V_a(\tau) = V_b(\tau)/2 = -\alpha(|\beta_{a,2}|/\beta_1\tau_0^2)\text{sech}^2(\tau/\tau_0)$ and a dispersion $\rho = \beta_{2,b}/\beta_{2,a}$, we have [100]

$$\Psi_{a,0} = c_a \text{sech}^{q_a}(\tau/\tau_0) \quad \Psi_{b,0} = c_b \text{sech}^{q_b}(\tau/\tau_0), \quad (\text{D10})$$

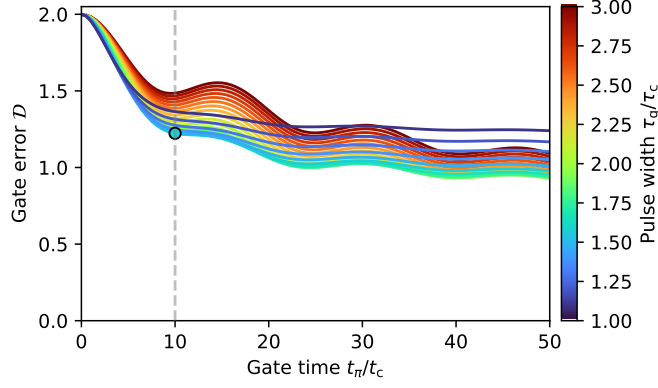


FIG. 6. Gate performance of a Kerr-phase gate \hat{U}_π implemented using Gaussian pulses shown for various gate times t_π and pulse widths τ_g . The gate error is measured as the distance \mathcal{D} between the output state $|\psi_{\text{out}}\rangle = e^{-i\hat{H}t_\pi} |2_{\text{in}}\rangle$ and the target state $-|2_{\text{out}}\rangle$. The solid circle represents the gate implementation with $\tau_g/\tau_c = 1.5$ that maximizes the performance for a gate time of $t_\pi/t_c = 10$. We assume $\omega_{b,0} - 2\omega_{a,0} = 0$ and $\beta_{a,2} = \beta_{b,2}/2$ for the simulation, and the system size T is taken large enough compared to the pulse width τ_g such that there is no boundary effect.

where c_u are normalization constants, and q_a and q_b are given as positive solutions of equations $q_a(q_a + 1)/2 = \alpha$ and $q_b(q_b + 1)/2 = 2\alpha/\rho$, respectively (Notice that $\alpha = 1$ and $\rho = 2$ corresponds to the case discussed in the main text). When the phase-mismatch is set to $\omega_{b,0} - 2\omega_{a,0} = (|\beta_{b,2}|q_b^2 - 2|\beta_{a,2}|q_a^2)/2\tau_0^2\beta_1$, the system Hamiltonian effectively reduces to the form (D9) with

$$g = \frac{r}{\pi^{1/4}\sqrt{\tau_0}} \frac{\Gamma(q_a + 1/2)\Gamma(q_a + q_b/2)\Gamma^{1/2}(q_b + 1/2)}{\Gamma^2(q_a)\Gamma(q_a + q_b/2 + 1/2)\Gamma^{1/2}(q_b)}, \quad (\text{D11})$$

where $\Gamma(x)$ is the Gamma function.

APPENDIX E: EXPERIMENTAL DETERMINATION OF THE NONLINEAR COUPLING

In this section, we derive expressions relating the nonlinear coupling g in the quantum model (2) to experimentally measurable parameters, e.g., the normalized SHG conversion efficiency and the threshold power for optical parametric oscillation. These formulas are used in the main text to estimate the figure of merit g/κ from devices presented in the literature. For the following, we consider a phase-matched $\chi^{(2)}$ resonator with a Hamiltonian

$$\frac{\hbar g}{2}(\hat{a}^{\dagger 2}\hat{b} + \hat{a}^2\hat{b}^{\dagger}), \quad (\text{E1})$$

where we explicitly denote the reduced Planck constant by \hbar . For both harmonics ($u \in \{a, b\}$), we denote the intrinsic and outcoupling decay rates by $\kappa_{u,\text{int}}$ and $\kappa_{u,\text{oc}}$, respectively.

We first consider resonant SHG pumped by an external FH drive with power $P_{\text{in}}^{(a)}$, which can be modeled by a Hamiltonian term $\hbar\epsilon_a(\hat{a} + \hat{a}^\dagger)$ with $\epsilon_a = \sqrt{2\kappa_{a,\text{oc}}P_{\text{in}}/\hbar\omega_{a,0}}$. Under c-number substitution $\hat{a} \mapsto \alpha$ and $\hat{b} \mapsto \beta$, the classical dynamics of the fields follow

$$i\partial_t\alpha = g\alpha^*\beta - i\kappa_a\alpha + \epsilon_a, \quad i\partial_t\beta = \frac{g}{2}\alpha^2 - i\kappa_b\beta, \quad (\text{E2})$$

where $\kappa_u = \kappa_{u,\text{int}} + \kappa_{u,\text{oc}}$ is the total loss rate. In the undepleted-pump regime, the steady-state populations are

$$|\alpha|^2 = \frac{\epsilon_a^2}{\kappa_a^2}, \quad |\beta|^2 = \frac{g^2}{4} \frac{|\alpha|^4}{\kappa_b^2}. \quad (\text{E3})$$

Using the steady-state values, we can relate the normalized SHG conversion efficiency $\eta_{\text{norm}} = P_{\text{out}}/P_{\text{in}}^2$ with the output SH power $P_{\text{out}} = 2\hbar\omega_{b,0}\kappa_{b,\text{oc}}|\beta|^2$ to the coupling coefficient g as

$$\eta_{\text{norm}} = \frac{4g^2}{\hbar\omega_{a,0}} \frac{\kappa_{b,\text{oc}}}{\kappa_b^2} \left(\frac{\kappa_{a,\text{oc}}}{\kappa_a^2} \right)^2. \quad (\text{E4})$$

More general expressions for η_{norm} in the case of the finite phase mismatch can be found in Ref. [23].

Next, let us consider the scenario where the cavity is pumped by an external SH drive with power P_{in} . When the pump power is larger than some threshold value P_{th} , the system undergoes optical parametric oscillation (OPO). The external SH drive can be modeled by a Hamiltonian term $\hbar\epsilon_b(\hat{b} + \hat{b}^\dagger)$ with $\epsilon_b = \sqrt{2\kappa_{b,\text{oc}}P_{\text{in}}/\hbar\omega_{b,0}}$, leading to classical equation of motions

$$i\partial_t\alpha = g\alpha^*\beta - i\kappa_a\alpha \quad i\partial_t\beta = \frac{g}{2}\alpha^2 - i\kappa_b\beta + \epsilon_b. \quad (\text{E5})$$

The steady-state population of the FH mode takes a finite value under the condition

$$P_{\text{in}} \geq \frac{\hbar\omega_{b,0}\kappa_a^2\kappa_b^2}{g^2\kappa_{b,\text{oc}}} = P_{\text{th}}, \quad (\text{E6})$$

which defines the OPO threshold power P_{th} . In particular, at critical coupling where $\kappa_{u,\text{int}} = \kappa_{u,\text{oc}}$, we have $P_{\text{th}} = 2\hbar\omega_{b,0}\kappa_a^2\kappa_b/g^2$. Alternatively, some experimental results are reported in terms of the “SHG saturation power” related to the OPO threshold by $P_{\text{sat}} = 4P_{\text{th}}$ [70], which also allows us to calculate g based on measurements of P_{sat} [48, 69].

-
- [1] H.-L. Yin, T.-Y. Chen, Z.-W. Yu, H. Liu, L.-X. You, Y.-H. Zhou, S.-J. Chen, Y. Mao, M.-Q. Huang, W.-J. Zhang, H. Chen, M. Jun Li, D. Nolan, F. Zhou, X. Jiang, Z. Wang, Q. Zhang, X.-B. Wang, and J.-W. Pan, Measurement-device-independent quantum key distribution over a 404 km optical fiber, *Phys. Rev. Lett.* **117**, 190501 (2016).
 - [2] H. J. Kimble, The quantum internet, *Nature* **453**, 1023 (2008).
 - [3] The LIGO Scientific Collaboration, Enhanced sensitivity of the LIGO gravitational wave detector by using squeezed states of light, *Nat. Photon.* **7**, 613 (2013).
 - [4] J. L. O’Brien, A. Furusawa, and J. Vučković, Photonic quantum technologies, *Nat. Photon.* **3**, 687 (2009).
 - [5] W. Asavanant, Y. Shiozawa, S. Yokoyama, B. Charoensombutamon, H. Emura, R. N. Alexander, S. Takeda, J. Yoshikawa, N. C. Menicucci, H. Yonezawa, and A. Furusawa, Generation of time-domain-multiplexed two-dimensional cluster state, *Science* **366**, 373 (2019).
 - [6] J. L. O’Brien, Optical Quantum Computing, *Science* **318**, 1567 (2007).
 - [7] E. Knill, R. Laflamme, and G. J. Milburn, A scheme for efficient quantum computation with linear optics, *Nature* **409**, 46 (2001).
 - [8] E. Knill, Quantum gates using linear optics and postselection, *Phys. Rev. A* **66**, 052306 (2002).
 - [9] R. Raussendorf and H. J. Briegel, A One-Way Quantum Computer, *Phys. Rev. Lett.* **86**, 5188 (2001).
 - [10] M. Nielsen, Optical Quantum Computation Using Cluster States, *Phys. Rev. Lett.* **93**, 040503 (2004).
 - [11] S. Slussarenko and G. J. Pryde, Photonic quantum information processing: A concise review, *Appl. Phys. Rev.* **6**, 041303 (2019).
 - [12] Y. Li, P. C. Humphreys, G. J. Mendoza, and S. C. Benjamin, Resource costs for fault-tolerant linear optical quantum computing, *Phys. Rev. X* **5**, 041007 (2015).
 - [13] P. Kok, W. J. Munro, K. Nemoto, T. C. Ralph, J. P. Dowling, and G. J. Milburn, Linear optical quantum computing with photonic qubits, *Rev. Mod. Phys.* **79**, 135 (2007).
 - [14] T. Rudolph, Why I am optimistic about the silicon-photonics route to quantum computing, *APL Photonics* **2**, 030901 (2017).
 - [15] G. J. Milburn, Quantum optical Fredkin gate, *Phys. Rev. Lett.* **62**, 2124 (1989).
 - [16] I. L. Chuang and Y. Yamamoto, Simple quantum computer, *Phys. Rev. A* **52**, 3489 (1995).
 - [17] N. K. Langford, S. Ramelow, R. Prevedel, W. J. Munro, G. J. Milburn, and A. Zeilinger, Efficient quantum computing using coherent photon conversion, *Nature* **478**, 360 (2011).
 - [18] T. Yoshie, A. Scherer, J. Hendrickson, G. Khitrova, H. Gibbs, G. Rupper, C. Ell, O. Shchekin, and D. Deppe, Vacuum Rabi splitting with a single quantum dot in a photonic crystal nanocavity, *Nature* **432**, 200 (2004).
 - [19] K. M. Birnbaum, A. Boca, R. Miller, A. D. Boozer, T. E. Northup, and H. J. Kimble, Photon blockade in an optical cavity with one trapped atom, *Nature* **436**, 87 (2005).
 - [20] D. Englund, A. Faraon, I. Fushman, N. Stoltz, P. Petroff, and J. Vučković, Controlling cavity reflectivity with a single quantum dot, *Nature* **450**, 857 (2007).
 - [21] B. Hacker, S. Welte, G. Rempe, and S. Ritter, A photon-photon quantum gate based on a single atom in an optical resonator, *Nature* **536**, 193 (2016).
 - [22] M. Zhang, C. Wang, R. Cheng, A. Shams-Ansari, and M. Lončar, Monolithic ultra-high-Q lithium niobate microring resonator, *Optica* **4**, 1536 (2017).
 - [23] J. Lu, M. Li, C.-L. Zou, A. Al Sayem, and H. X. Tang, Towards 1% single photon nonlinearity with periodically-poled lithium niobate microring resonators, *Optica* **7**, 1654 (2020).
 - [24] G. P. Agrawal, Nonlinear fiber optics, in *Nonlinear Science at the Dawn of the 21st Century* (Springer, 2000) pp. 195–211.
 - [25] M. Jankowski, J. Mishra, and M. M. Fejer, Dispersion-engineered $\chi^{(2)}$ nanophotonics: a flexible tool for nonclassical light, *J. Phys. Photon.* **3**, 042005 (2021).
 - [26] J. H. Shapiro, Single-photon Kerr nonlinearities do not help quantum computation, *Phys. Rev. A* **73**, 062305 (2006).

- (2006).
- [27] J. H. Shapiro and M. Razavi, Continuous-time cross-phase modulation and quantum computation, *New J. Phys.* **9**, 16 (2007).
 - [28] A. Marandi, Z. Wang, K. Takata, R. L. Byer, and Y. Yamamoto, Network of time-multiplexed optical parametric oscillators as a coherent Ising machine, *Nat. Photonics* **8**, 937 (2014).
 - [29] A. Crespi, R. Ramponi, R. Osellame, L. Sansoni, I. Bongioanni, F. Sciarrino, G. Vallone, and P. Mataloni, Integrated photonic quantum gates for polarization qubits, *Nat. Commun.* **2**, 566 (2011).
 - [30] P. C. Humphreys, B. J. Metcalf, J. B. Spring, M. Moore, X.-M. Jin, M. Barbieri, W. S. Kolthammer, and I. A. Walmsley, Linear Optical Quantum Computing in a Single Spatial Mode, *Phys. Rev. Lett.* **111**, 150501 (2013).
 - [31] X. Qiang, X. Zhou, J. Wang, C. M. Wilkes, T. Loke, S. O’Gara, L. Kling, G. D. Marshall, R. Santagati, T. C. Ralph, J. B. Wang, J. L. O’Brien, M. G. Thompson, and J. C. F. Matthews, Large-scale silicon quantum photonics implementing arbitrary two-qubit processing, *Nat. Photon.* **12**, 534 (2018).
 - [32] J. L. O’Brien, G. J. Pryde, A. G. White, T. C. Ralph, and D. Branning, Demonstration of an all-optical quantum controlled-NOT gate, *Nature* **426**, 264 (2003).
 - [33] C. K. Hong, Z. Y. Ou, and L. Mandel, Measurement of subpicosecond time intervals between two photons by interference, *Phys. Rev. Lett.* **59**, 2044 (1987).
 - [34] K. Rivoire, S. Buckley, and J. Vučković, Multiply resonant photonic crystal nanocavities for nonlinear frequency conversion, *Opt. Express* **19**, 22198 (2011).
 - [35] M. Minkov, D. Gerace, and S. Fan, Doubly resonant $\chi^{(2)}$ nonlinear photonic crystal cavity based on a bound state in the continuum, *Optica* **6**, 1039 (2019).
 - [36] Z. Lin, X. Liang, M. Lončar, S. G. Johnson, and A. W. Rodriguez, Cavity-enhanced second-harmonic generation via nonlinear-overlap optimization, *Optica* **3**, 233 (2016).
 - [37] Z. Lin, M. Lončar, and A. W. Rodriguez, Topology optimization of multi-track ring resonators and 2D microcavities for nonlinear frequency conversion, *Opt. Lett.* **42**, 2818 (2017).
 - [38] Q. Quan and M. Lončar, Deterministic design of wavelength scale, ultra-high Q photonic crystal nanobeam cavities, *Opt. Express* **19**, 18529 (2011).
 - [39] T. Asano and S. Noda, Iterative optimization of photonic crystal nanocavity designs by using deep neural networks, *Nanophotonics* **8**, 2243 (2019).
 - [40] H. Sekoguchi, Y. Takahashi, T. Asano, and S. Noda, Photonic crystal nanocavity with a Q-factor of 9 million, *Opt. Express* **22**, 916 (2014).
 - [41] M. Minkov and V. Savona, Automated optimization of photonic crystal slab cavities, *Sci. Rep.* **4**, 5124 (2014).
 - [42] T. Asano, Y. Ochi, Y. Takahashi, K. Kishimoto, and S. Noda, Photonic crystal nanocavity with a Q factor exceeding eleven million, *Opt. Express* **25**, 1769 (2017).
 - [43] D. Dodane, J. Bourderionnet, S. Combrié, and A. de Rossi, Fully embedded photonic crystal cavity with Q=0.6 million fabricated within a full-process CMOS multiproject wafer, *Opt. Express* **26**, 20868 (2018).
 - [44] Y. Taguchi, Y. Takahashi, Y. Sato, T. Asano, and S. Noda, Statistical studies of photonic heterostructure nanocavities with an average Q factor of three million, *Opt. Express* **19**, 11916 (2011).
 - [45] A. Shams-Ansari, G. Huang, L. He, M. Churayev, P. Kharel, Z. Tan, J. Holzgrafe, R. Cheng, D. Zhu, J. Liu, B. Desiatov, M. Zhang, T. J. Kippenberg, and M. Lončar, Probing the limits of optical loss in ion-sliced thin-film lithium niobate, in *CLEO: Science and Innovations* (Optical Society of America, 2021) pp. STh4J–4.
 - [46] R. Gao, H. Zhang, F. Bo, W. Fang, Z. Hao, N. Yao, J. Lin, J. Guan, L. Deng, M. Wang, L. Qiao, and Y. Cheng, Broadband highly efficient nonlinear optical processes in on-chip integrated lithium niobate microdisk resonators of Q-factor above 10^8 , *New J. Phys.* **23**, 123027 (2021).
 - [47] R. Gao, N. Yao, J. Guan, L. Deng, J. Lin, M. Wang, L. Qiao, W. Fang, and Y. Cheng, Lithium niobate microring with ultra-high Q factor above 10^8 , *Chin. Opt. Lett.* **20**, 011902 (2022).
 - [48] V. S. Ilchenko, A. A. Savchenkov, A. B. Matsko, and L. Maleki, Nonlinear optics and crystalline whispering gallery mode cavities, *Phys. Rev. Lett.* **92**, 043903 (2004).
 - [49] D. Serkland, R. Eckardt, and R. Byer, Continuous-wave total-internal-reflection optical parametric oscillator pumped at 1064 nm, *Opt. Lett.* **19**, 1046 (1994).
 - [50] A. A. Savchenkov, V. S. Ilchenko, A. B. Matsko, and L. Maleki, Kilohertz optical resonances in dielectric crystal cavities, *Phys. Rev. A* **70**, 051804(R) (2004).
 - [51] J. R. Schwesyg, M. C. C. Kajiyama, M. Falk, D. H. Jundt, K. Buse, and M. M. Fejer, Light absorption in undoped congruent and magnesium-doped lithium niobate crystals in the visible wavelength range, *Appl. Phys. B* **100**, 109 (2010).
 - [52] N. Quesada, L. G. Helt, M. Menotti, M. Liscidini, and J. E. Sipe, Beyond photon pairs: Nonlinear quantum photonics in the high-gain regime (2021), arXiv:2110.04340 [quant-ph].
 - [53] L. A. Lugiato and R. Lefever, Spatial dissipative structures in passive optical systems, *Phys. Rev. Lett.* **58**, 2209 (1987).
 - [54] T. P. McKenna, H. S. Stokowski, V. Ansari, J. Mishra, M. Jankowski, C. J. Sarabalis, J. F. Herrmann, C. Langrock, M. M. Fejer, and A. H. Safavi-Naeini, Ultra-low-power second-order nonlinear optics on a chip (2021), arXiv:2102.05617 [physics.optics].
 - [55] K. Nemoto and W. J. Munro, Nearly deterministic linear optical controlled-not gate, *Phys. Rev. Lett.* **93**, 250502 (2004).
 - [56] K. Fukui, M. Endo, W. Asavanant, A. Sakaguchi, J. Yoshikawa, and A. Furusawa, Generating the Gottesman-Kitaev-Preskill qubit using a cross-Kerr interaction between squeezed light and Fock states in optics, *Phys. Rev. A* **105**, 022436 (2022).
 - [57] J. J. Sakurai and J. Napolitano, *Modern Quantum Mechanics* (Cambridge University Press, 2017).
 - [58] H. Carmichael, *An open systems approach to quantum optics: lectures presented at the Université Libre de Bruxelles, October 28 to November 4, 1991*, Vol. 18 (Springer Science & Business Media, 2009).
 - [59] M. Heuck, K. Jacobs, and D. R. Englund, Photon-photon interactions in dynamically coupled cavities,

- Phys. Rev. A **101**, 042322 (2020).
- [60] M. Heuck, K. Jacobs, and D. R. Englund, Controlled-Phase Gate Using Dynamically Coupled Cavities and Optical Nonlinearities, *Phys. Rev. Lett.* **124**, 160501 (2020).
 - [61] J. A. Medina-Vázquez, E. Y. González-Ramírez, and J. G. Murillo-Ramírez, Photonic crystal meso-cavity with double resonance for second-harmonic generation, *J. Phys. B: At. Mol. Opt. Phys.* **54**, 245401 (2022).
 - [62] J.-Y. Chen, C. Tang, M. Jin, Z. Li, Z. Ma, H. Fan, S. Kumar, Y. M. Sua, and Y.-P. Huang, Efficient Frequency Doubling with Active Stabilization on Chip, *Laser Photonics Rev.* **15**, 2100091 (2021).
 - [63] J.-Y. Chen, Z. Li, Z. Ma, C. Tang, H. Fan, Y. M. Sua, and Y.-P. Huang, Photon Conversion and Interaction on Chip (2021), arXiv:2105.00275 [physics.optics].
 - [64] J. Wang, M. Clementi, M. Minkov, A. Barone, J.-F. Carlin, N. Grandjean, D. Gerace, S. Fan, M. Galli, and R. Houdré, Doubly resonant second-harmonic generation of a vortex beam from a bound state in the continuum, *Optica* **7**, 1126 (2020).
 - [65] Z. Ma, J.-Y. Chen, Z. Li, C. Tang, Y. M. Sua, H. Fan, and Y.-P. Huang, Ultrabright Quantum Photon Sources on Chip, *Phys. Rev. Lett.* **125**, 263602 (2020).
 - [66] L. Chang, A. Boes, P. Pintus, J. D. Peters, M. Kennedy, X.-W. Guo, N. Volet, S.-P. Yu, S. B. Papp, and J. E. Bowers, Strong frequency conversion in heterogeneously integrated GaAs resonators, *APL Photon.* **4**, 036103 (2019).
 - [67] J.-Y. Chen, Z.-H. Ma, Y. M. Sua, Z. Li, C. Tang, and Y.-P. Huang, Ultra-efficient frequency conversion in quasi-phase-matched lithium niobate microrings, *Optica* **6**, 1244 (2019).
 - [68] A. W. Bruch, X. Liu, X. Guo, J. B. Surya, Z. Gong, L. Zhang, J. Wang, J. Yan, and H. X. Tang, 17000%/W second-harmonic conversion efficiency in single-crystalline aluminum nitride microresonators, *Appl. Phys. Lett.* **113**, 131102 (2018).
 - [69] D. V. Fürst, Strekalov, D. Elser, M. Lassen, U. L. Andersen, C. Marquardt, and G. Leuchs, Naturally Phase-Matched Second-Harmonic Generation in a Whispering-Gallery-Mode Resonator, *Phys. Rev. Lett.* **104**, 153901 (2010).
 - [70] J. U. Fürst, D. V. Strekalov, D. Elser, A. Aiello, U. L. Andersen, C. Marquardt, and G. Leuchs, Low-Threshold Optical Parametric Oscillations in a Whispering Gallery Mode Resonator, *Phys. Rev. Lett.* **105**, 263904 (2010).
 - [71] T. Park, H. S. Stokowski, V. Ansari, T. P. McKenna, A. Y. Hwang, M. M. Fejer, and A. H. Safavi-Naeini, High efficiency second harmonic generation of blue light on thin film lithium niobate (2021), arXiv:2108.06398 [physics.optics].
 - [72] R. Bhatt, I. Bhaumik, S. Ganesamoorthy, A. K. Karnal, M. K. Swami, H. S. Patel, and P. K. Gupta, Urbach tail and bandgap analysis in near stoichiometric LiNbO₃ crystals, *Phys. Status Solidi (a)* **209**, 176 (2011).
 - [73] B. Desiatov, A. Shams-Ansari, M. Zhang, C. Wang, and M. Lončar, Ultra-low-loss integrated visible photonics using thin-film lithium niobate, *Optica* **6**, 380 (2019).
 - [74] M. Leidinger, S. Fieberg, N. Waasem, F. Kühnemann, K. Buse, and I. Breunig, Comparative study on three highly sensitive absorption measurement techniques characterizing lithium niobate over its entire transparent spectral range, *Opt. Express* **23**, 21690 (2015).
 - [75] J. Liu, A. S. Raja, M. Karpov, B. Ghadiani, M. H. P. Pfeiffer, B. Du, N. J. Engelsen, H. Guo, M. Zervas, and T. J. Kippenberg, Ultralow-power chip-based soliton microcombs for photonic integration, *Optica* **5**, 1347 (2018).
 - [76] W. T. Irvine, K. Hennessy, and D. Bouwmeester, Strong coupling between single photons in semiconductor microcavities, *Phys. Rev. Lett.* **96**, 057405 (2006).
 - [77] A. Majumdar and D. Gerace, Single-photon blockade in doubly resonant nanocavities with second-order nonlinearity, *Phys. Rev. B* **87**, 235319 (2013).
 - [78] D. Gottesman, A. Kitaev, and J. Preskill, Encoding a qubit in an oscillator, *Phys. Rev. A* **64**, 012310 (2001).
 - [79] N. C. Menicucci, P. van Loock, M. Gu, C. Weedbrook, T. C. Ralph, and M. A. Nielsen, Universal Quantum Computation with Continuous-Variable Cluster States, *Phys. Rev. Lett.* **97**, 110501 (2006).
 - [80] R. Yanagimoto, T. Onodera, E. Ng, L. G. Wright, P. L. McMahon, and H. Mabuchi, Engineering a Kerr-Based Deterministic Cubic Phase Gate via Gaussian Operations, *Phys. Rev. Lett.* **124**, 240503 (2020).
 - [81] Y. Zheng, O. Hahn, P. Stadler, P. Holmval, F. Quijandría, A. Ferraro, and G. Ferrini, Gaussian Conversion Protocols for Cubic Phase State Generation, *PRX Quantum* **2**, 010327 (2021).
 - [82] J. M. Arrazola, T. R. Bromley, J. Izaac, C. R. Myers, K. Brádler, and N. Killoran, Machine learning method for state preparation and gate synthesis on photonic quantum computers, *Quantum Sci. Technol.* **4**, 024004 (2019).
 - [83] J. E. Bourassa, R. N. Alexander, M. Vasmer, A. Patil, I. Tzitrin, T. Matsuura, D. Su, B. Q. Baragiola, S. Guha, G. Dauphinais, K. K. Sabapathy, N. C. Menicucci, and I. Dhand, Blueprint for a scalable photonic fault-tolerant quantum computer, *Quantum* **5**, 392 (2021).
 - [84] B. Brecht, D. V. Reddy, C. Silberhorn, and M. G. Raymer, Photon Temporal Modes: A Complete Framework for Quantum Information Science, *Phys. Rev. X* **5**, 041017 (2015).
 - [85] B. Brecht, A. Eckstein, A. Christ, and C. Silberhorn, From quantum pulse gate to quantum pulse shaper—engineered frequency conversion in nonlinear optical waveguides, *New J. Phys.* **13**, 065029 (2011).
 - [86] T. Inagaki, K. Inaba, R. Hamerly, K. Inoue, Y. Yamamoto, and H. Takesue, Large-scale ising spin network based on degenerate optical parametric oscillators, *Nat. Photonics* **10**, 415 (2016).
 - [87] P. D. Drummond, Electromagnetic quantization in dispersive inhomogeneous nonlinear dielectrics, *Phys. Rev. A* **42**, 6845 (1990).
 - [88] M. G. Raymer, Quantum theory of light in a dispersive structured linear dielectric: a macroscopic Hamiltonian tutorial treatment, *J. Mod. Opt.* **67**, 196 (2020).
 - [89] N. Quesada and J. E. Sipe, Why you should not use the electric field to quantize in nonlinear optics, *Opt. Lett.* **42**, 3443 (2017).
 - [90] A. Rodriguez, M. Soljačić, J. D. Joannopoulos, and S. G. Johnson, $\chi^{(2)}$ and $\chi^{(3)}$ harmonic generation at a critical power in inhomogeneous doubly resonant cavities, *Opt. Express* **15**, 7303 (2007).

- [91] J. D. Joannopoulos, S. G. Johnson, J. N. Winn, and R. D. Meade, *Photonic crystals* (Princeton university press, 2011).
- [92] R. W. Boyd, *Nonlinear Optics, 3rd edition* (Academic Press, 2008).
- [93] S. Hu and S. M. Weiss, Design of photonic crystal cavities for extreme light concentration, *ACS Photonics* **3**, 1647 (2016).
- [94] H. Choi, M. Heuck, and D. Englund, Self-similar nanocavity design with ultrasmall mode volume for single-photon nonlinearities, *Phy. Rev. Lett.* **118**, 223605 (2017).
- [95] K. R. Parameswaran, R. K. Route, J. R. Kurz, R. V. Roussev, M. M. Fejer, and M. Fujimura, Highly efficient second-harmonic generation in buried waveguides formed by annealed and reverse proton exchange in periodically poled lithium niobate, *Opt. Lett.* **27**, 179 (2002).
- [96] S. Kurimura, Y. Kato, M. Maruyama, Y. Usui, and H. Nakajima, Quasi-phase-matched adhered ridge waveguide in LiNbO₃, *Appl. Phys. Lett.* **89**, 191123 (2006).
- [97] C. Wang, C. Langrock, A. Marandi, M. Jankowski, M. Zhang, B. Desiatov, M. M. Fejer, and M. Lončar, Ultrahigh-efficiency wavelength conversion in nanophotonic periodically poled lithium niobate waveguides, *Optica* **5**, 1438 (2018).
- [98] R. Yanagimoto, E. Ng, L. G. Wright, T. Onodera, and H. Mabuchi, Efficient simulation of ultrafast quantum nonlinear optics with matrix product states, *Optica* **8**, 1306 (2021).
- [99] R. Yanagimoto, E. Ng, A. Yamamura, T. Onodera, L. G. Wright, M. Jankowski, M. M. Fejer, P. L. McMahon, and H. Mabuchi, Onset of non-Gaussian quantum physics in pulsed squeezing with mesoscopic fields (2021), arXiv:2111.13799 [quant-ph].
- [100] J. T. Manassah, Ultrafast solitary waves sustained through induced phase modulation by a copropagating pump, *Opt. Lett.* **15**, 670 (1990).